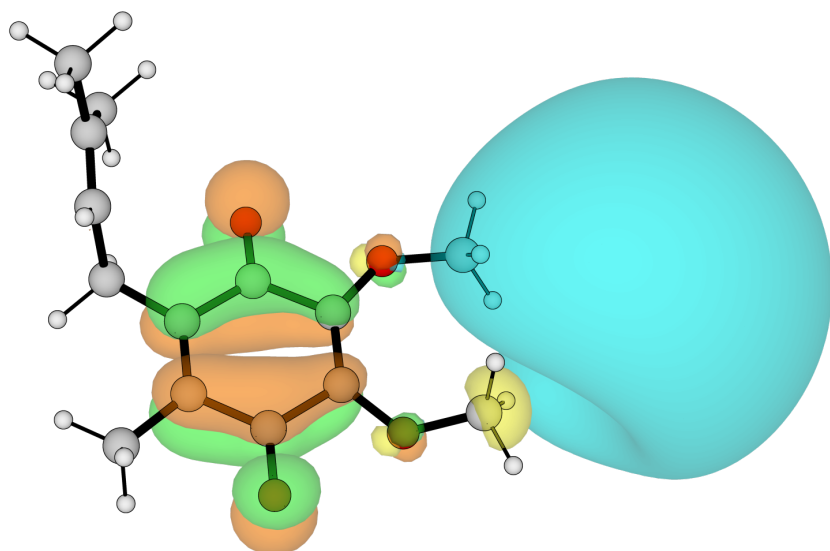


Computational Exploration of Non-Valence Anions from Biological Quinones



Mauro GASCÓN

Supervisor: Prof. Thomas C. Jagau
KU Leuven

Mentor: Robin E. Moorby
KU Leuven

Thesis presented in
fulfilment of the requirements
for the degree of Master of Science
in Theoretical Chemistry and Computational Modelling

Academic year 2024-2025

© Copyright by KU Leuven

Without written permission of the promtors and the authors it is forbidden to reproduce or adapt in any form or by any means any part of this publication. Requests for obtaining the right to reproduce or utilize parts of this publication should be addressed to KU Leuven, Faculteit Wetenschappen, Celestijnenlaan 200H bus 2100, 3001 Leuven (Heverlee), telephone +32 16 32 14 01.

A written permission of the promotor is also required to use the methods, products, schematics and programs described in this work for industrial or commercial use, and for submitting this publication in scientific contests.

This thesis is an exam document that obtained no further correction of possible errors after the defense. Referring to this thesis in papers and analogous documents is only allowed after written consent of the supervisor(s), mentioned on the title page.

Acknowledgements

Thank you thank you.

Abstract

The redox reactions of ubiquinone (CoQ) are a key step in cellular respiration. CoQ, is able to support two anionic states; a valence-bound (VBS) and non-valence dipole-bound state (DBS). In DBSs the excess electron is weakly bound by the molecular dipole, and have sparked interest as potential ‘doorways’ for electron transfer processes. However, their theoretical study is challenging due to the diffuse nature of the electron cloud and sensitivity to electron correlation.

In this work, the cost-effective electron-attachment equation-of-motion second-order approximated coupled-cluster method (EA-EOM-CC2) is used to study the anionic states of CoQ. Firstly, EA-EOM-CC2 is benchmarked and validated for calculating electron affinities of both VBSs and DBSs anions. Moreover, Dyson orbitals for EOM-CC2 are implemented, providing a tool for characterizing electron attachment/detachment processes and calculating properties like photodetachment cross-sections.

CoQ analogues, Q₀ (2,3-dimethoxy-5-methyl-*p*-benzoquinone) and Q₁ (Q₀ with one isoprene unit at position 6), are investigated, revealing a strong interplay between the conformation of the methoxy chains and the stability of the DBS, mediated by changes in the molecular dipole moment. It is shown that the relative orientation of the dipole is as important as its strength to the electron binding energy. The polarity of the local molecular environment on these anionic states is shown to have a strong effect on both anionic states. This research enhances the understanding of how structural and solvent factors govern the electron transfer processes in biologically relevant quinones, providing insights on how the local protein environment could favour or disfavour the existence of non-valence states.

Beknopte samenvatting

De redoxreacties van ubiquinon (CoQ) vormen een essentiële stap in de cellulaire respiratioe. CoQ is in staat om twee anionische toestanden te ondersteunen: een valentiegebonden toestand (VBS) en een niet-valentiegebonden dipoolgebonden toestand (DBS). In DBS'ën wordt het overtollige elektron zwak gebonden door de moleculaire dipool, wat deze toestanden bijzonder interessant maakt als mogelijke ‘toegangspoorten’ voor elektronentransferprocessen. Hun theoretische studie blijft echter een uitdaging, vanwege de diffuse aard van de elektronenwolk en de gevoeligheid voor elektronencorrelatie.

In deze studie wordt de kostenefficiënte ‘electron-attachment equation-of-motion second-order approximate coupled-cluster’ methode (EA-EOM-CC2) toegepast om de anionische toestanden van CoQ te onderzoeken. Eerst wordt EA-EOM-CC2 gebenchmarkt en gevalideerd voor het berekenen van de elektronaffiniteiten van zowel VBS- als DBS-anionen. Daarnaast worden Dyson-orbitalen geïmplementeerd binnen het EOM-CC2-formalisme, wat een waardevol instrument biedt voor het karakteriseren van elektron aanhechtings en verwijderings processen, evenals voor het berekenen van eigenschappen zoals elektron photoverwijderings doorsneden.

Twee CoQ-anologen worden onderzocht: Q₀ (2,3-dimethoxy-5-methyl-*p*-benzoquinon) en Q₁ (Q₀ met één isopreeneenheid op positie 6). De resultaten tonen een sterke wisselwerking aan tussen de conformatie van de methoxyketens en de stabiliteit van de DBS, gemedieerd door veranderingen in het moleculaire dipoolmoment. Er wordt aangetoond dat de relatieve oriëntatie van de dipool minstens even bepalend is als de sterkte ervan voor de bindingsenergie van het elektron. Tevens blijkt de polariteit van de lokale moleculaire omgeving een significante invloed uit te oefenen op beide anionische toestanden. Deze bevindingen dragen bij tot een beter begrip van structurele factoren en solventeffecten die elektronentransfer in biologisch relevante quinonen sturen, en bieden inzicht in hoe de lokale eiwitomgeving het bestaan van niet-valentiegebonden toestanden kan bevorderen of verhinderen.

List of abbreviations

NVS Non-Valence State

DBS Dipole-Bound State

VBS Valence-Bound State

QBS Quadrupole-Bound State

CBS Correlation-Bound State

EOM Equation-of-Motion

CC Coupled Cluster

CCSD Coupled Cluster with Single and Double excitations

CC2 Second-order approximate Coupled Cluster

HF Hartree-Fock

DFT Density Functional Theory

MP2 Møller–Plesset perturbation theory of second order

CoQ Coenzyme Q

uQ Ubiuinone

Q_n Ubiuinone with n isoprene units

ETC Electron Transport Chain

MO Molecular Orbital

EA Electron Affinity

QM Quantum Mechanics

Contents

Abstract	iv
Beknopte samenvatting	v
List of abbreviations	vi
1 Introduction	1
1.1 Non-Valence Anions	1
1.1.1 Dipole-Bound Anions	2
1.1.2 Approaches to Study Non-Valence Anions	3
1.1.3 Non-Valence Anions in Condensed Matter	4
1.1.4 Non-Valence Anions in Biological Systems	5
1.2 Ubiquinone	6
1.3 Research Goals	8
2 Theoretical Background	9
2.1 Ground State Electronic Structure Methods	9
2.1.1 Electron Correlation	10
2.1.2 Møller-Plesset Perturbation Theory	11
2.1.3 Density Functional Theory	11
2.1.4 Configuration Interaction	12
2.1.5 Coupled Cluster Theory	13
2.1.6 Second Approximate Coupled Cluster	14
2.2 Equation-of-Motion Methods	15
2.3 Dyson Orbitals	17
2.3.1 EOM-CC2 Dyson Orbital Equations	18
3 Computational Details	20
3.1 Performance Evaluation of EOM-CC2 Methods	20
3.1.1 Basis Set Dependence of EA-EOM-CC2 for Dipole-Bound Anions	20

3.1.2	Assessment of EA-EOM-CC2 for Valence-Bound Radical Anion States in Quinones	21
3.1.3	Photoelectron Cross-sections from EOM-CC2 and EOM-CCSD	21
3.2	Ubiquinone Computational Models	21
3.2.1	Potential Energy Surfaces of Quinone Models	21
3.2.2	Interaction Scans with Small Molecules	22
4	Results and Discussion	23
4.1	Performance of EOM-CC2 Methods	23
4.1.1	Basis Set Dependence of EA-EOM-CC2 in Dipole Bound Anions	23
4.1.2	Performance of EA-EOM-CC2 on Valence Bound Radical Anion States of Quinones	26
4.1.3	Photoelectron Cross-section from EOM-CC2/CCSD	27
4.2	Study on the Anion States of Ubiquinone	28
4.2.1	Energy and Dipole Surfaces of CoQ	29
4.2.2	Interaction with small molecules	35
5	Conclusion and Outlook	39
A	Algebraic Expressions for the Dyson Orbitals	48
B	Photoelectron Cross-sections	51

Chapter 1

Introduction

1.1 Non-Valence Anions

An anion is an atom or molecule possessing a negative charge^{1–4}. The binding of electrons to a molecule is a balance between the attractive potential between the electron and the nuclei, and the repulsive forces between the electrons. Because the equilibrium of charge is broken towards the negative side, the binding energy of the excess electron is typically significantly smaller in magnitude than the ionisation energy of the neutral molecule. Moreover, the properties of the anion can be very different from those of the neutral species, with differences ranging from the molecular structure to the chemical reactivity. This makes their consideration essential when studying chemical processes such as electrochemistry, catalysis, polymerization, charge transfer, ... In discussions of molecular anions, the concept of electron affinity (EA) is key. The adiabatic electron affinity (AEA) quantifies the energy difference between a molecule and its corresponding anion, both in their structural ground state and lowest vibrational levels. The vertical electron affinity (VEA), defined at the neutral equilibrium geometry, is particularly relevant for electron capture dynamics. A molecule with a positive EA is considered electronically stable, releasing energy when an electron is attached¹.

Molecular anions are classified into valence bound states (VBS), where the excess electron occupies a compact orbital similar to valence molecular orbitals, and non-valence states (NVS), where the excess electron occupies a diffuse orbital spatially separated from the molecule. Unlike valence electrons, these “extra” electrons do not experience a $-1/r$ Coulombic attraction at long distances. Instead, they interact through charge-multipole potentials, which are weaker than the covalent bonds holding the molecule together^{1,4}.

Non-valence anions can be categorised into dipole-bound states (DBS)^{5–9}, quadrupole-

bound states (QBS)^{10–12}, and correlation-bound states (CBS)^{13–16}. In DBSs, the excess electron is stabilised by the interaction with the molecule’s significant dipole moment. It is generally accepted that the minimum required dipole strength to support a DBS is 2.5 Debye⁸. QBSs, on the other hand, arise from electrostatic interactions involving a large quadrupole moment in molecules with no dipole moment. Unlike DBSs, no definitive critical quadrupole moment has been established for the formation of quadrupole-bound states¹². Lastly, CBSs are stabilised not by electrostatic forces but by dispersion interactions. It is worth noting that many DBSs and QBSs remain unbound if electron correlation effects are ignored, which blurs the distinction between these types of non-valence anions¹⁶. Examples of different anion types are shown in Figure 1.1.

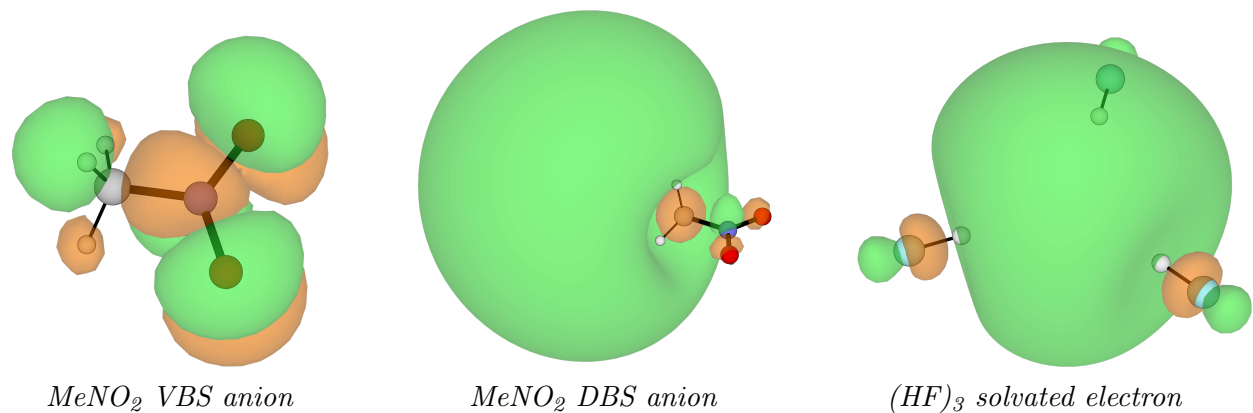


Figure 1.1: Dyson orbital for different types of anions computed using EA-EOM-CC2: a) Valence bound state of nitromethane anion, b) dipole bound state of nitromethane, c) solvated electron by a HF trimer. The isosurfaces are set to 0.005 a.u.

1.1.1 Dipole-Bound Anions

Of the different non-valence anions, DBSs are the most common and well-studied. They were first proposed in 1947, when it was demonstrated that an ideal dipole could bind an excess electron if the dipole moment exceeds 1.6 D⁵. Further studies regarding ‘real’ molecules, set the now generally accepted critical dipole moment of 2.5 D to bind an extra electron, although having a dipole moment above this threshold does not guarantee the formation of a dipole-bound anion.⁸.

The weak forces that bind the excess electron are responsible for the diffuse nature of the state, with the electronic density often extending several Ångströms away from the nuclei, and their relatively low binding energy, usually below 0.1 eV. This makes them susceptible to external perturbations, such as solvent interactions or electric fields, which

can significantly influence their stability and reactivity^{1,4,8,17–21}

DBSs possesses binding energies comparable to thermal energy ($k_bT \sim 23$ meV at room temperature), which might suggest limited practical relevance due to potential detachment. However, DBSs can play a significant role in systems that support both VBSs and NVSs. These systems can undergo a transition from a non-valence anion state to a stable valence state^{4,8}. Moreover, since the electron density of an NVS is spatially extended and resides far from the nuclei, the relaxed structure of an NVS is much closer to that of the neutral molecule compared to a VBS. This large spatial extent also results in a higher cross-section for electron capture and transfer. Consequently, DBSs can act as ‘doorway’ states, facilitating electron capture and transfer processes^{1,2,8,22–28}. This unique behavior has sparked interest in the role of NVSs across various fields, including astrochemistry²⁹ and radiobiology^{30–32}.

1.1.2 Approaches to Study Non-Valence Anions

Significant progress has been made in experimental and theoretical methods for elucidating the structure and dynamics of NVSs.^{1,2,33} Experimentally, dipole-bound anions are characterised using spectroscopic techniques designed to probe their weakly bound electronic states^{34–36}. In photodetachment and photoelectron spectroscopies, a beam of the target species is generated—often using a laser vaporisation or electrospray source—and probed with light. The energy of the ejected electrons reveals information about the vertical detachment energy and electronic structure of the state. Time-resolved photoelectron spectroscopy (TRPES)^{37,38} extends this approach, using ultrafast laser pulses to investigate the dynamics of electron attachment and detachment on femtosecond timescales, revealing transient states and relaxation pathways. DBSs can also be accessed by Rydberg electron transfer spectroscopy (RET)^{20,39,40}, which has been used to probe their role in electron transfer dynamics. Time-of-flight mass spectrometry is often coupled with these techniques to identify and isolate the correct anionic species^{6,41,42}.

The theoretical investigation of DBAs presents two main challenges. Firstly, the large spatial extent of the DB orbital requires atomic orbital basis sets that are sufficiently diffuse to accurately describe it, necessitating the use of large custom basis sets⁴³. Secondly, electron correlation is important; although the electron density at the valence level remains largely unchanged from the parent molecule, the non-valence part of the density is considerably polarisable due to its diffuse nature and exhibits significant dispersion-like interactions with the valence region, contributing substantially to the binding energy of

the extra electron^{1–3,7,16}.

Regarding computational methods, standard density functional theory (DFT) approaches can fail because most exchange-correlation functionals cannot properly describe dispersion interactions and can suffer from spin contamination in open-shell molecules⁴⁴. Multiconfigurational methods like complete active space self-consistent field (CASSCF)^{45,46} can capture the static correlation of the open shell systems, but require considerable effort in selecting an appropriate active space that balances accuracy and computational feasibility. Moreover, they lack dynamic correlation inherent in the dispersion. Currently, equation-of-motion coupled-cluster (EOM-CC)^{4,8,47} methods are often used for DBA modelling as they adequately treat both the electron correlation and open-shell character. However, the high computational cost of EOM-CC approaches significantly limits their applicability to small molecular systems. To address this, some approximate methods have been developed, such as the domain-based local pair natural orbital coupled-cluster theory (DLPNO) method^{48,49}, or the second order approximate CC2^{50,51}, which is used in this work.

1.1.3 Non-Valence Anions in Condensed Matter

Several studies have shown that individual molecules interacting with an NVS-hosting molecule can further stabilise the state by increasing the overall dipole moment or by combining their dipoles to collectively bind the electron within an intermolecular cavity. Moreover, in condensed phase, the excess electron can be stabilised by the interaction of multiple solvent molecules, rather than binding to an individual one, this situation is known as a solvated electron^{1,4,8,17,19–21}

The binding energy of such solvated electrons can increase dramatically with cluster size. A water molecule does not support any bound anionic state⁴, however a water dimer anion (H_2O)₂⁻ exhibits a low vertical detachment energy (VDE) of 45 meV⁵². Water cluster anions (H_2O)_n⁻ made of *ca.* 100 molecules can achieve VDEs exceeding 2.0 eV⁵³, and in bulk this values is measured to be between 3.4 and 4 eV^{54,55}. The structure of the state was the subject of much debate in the literature^{56–59}, but it is now generally accepted that the excess electron resides in a cavity of approximately 2.5 Å in size⁵⁷. This illustrates how solvent molecules can transform a weakly bound non-valence state into a strongly bound electronic species, though with significantly altered properties.

For solutes, the existence of hydrated NVSs still remains a subject of discussion^{60–62}.

Computational studies suggest that hydration influences the localisation of the excess electron, often displacing it onto the surface of the solvent cage⁶⁰. Conversely, experimental evidence indicates that alkyl chains do not disrupt DBS stability⁶¹, and DBS-mediated mechanisms have been observed in solvated uracil systems⁶³. The viability of NVS in bulk systems depends on the molecular density and polarity of the medium. While solvents may hinder DBS existence due to excluded volume effects, they can also stabilise DBS through Van der Waals interactions^{40,64}. Distinct scenarios can be considered in the interaction between a DBA supporting molecule and solvent: the electron may be found in the NVS orbital, captured by the solvent, or at the interface of the solute and solvent. The latter two phenomena are linked to charge-transfer-to-solvent (CTTS) electronic transitions and are observed experimentally^{40,64–66}.

1.1.4 Non-Valence Anions in Biological Systems

Research on dipole-bound anions (DBAs) has predominantly focused on gas-phase systems. However, in biological contexts, DBAs have garnered attention due to their interactions with DNA, particularly in the context of radiation-induced damage and radiosensitizers^{30–32}. When high-energy radiation interacts with biological samples, it generates a cascade of secondary electrons which can be captured by cellular constituents, potentially through non-valence states. It has been hypothesised that NVSs in DNA act as electron scavengers, leading to strand breaks and other forms of damage^{25,30,31,63}. Radiosensitizers are drugs designed to enhance the efficacy of radiation therapy in cancer treatment. These compounds become cytotoxic upon capturing secondary electrons generated during radiation exposure, potentially through the formation of NVSs³².

The role of NVSs in natural biological pathways beyond genetic damage remains largely unexplored, although it has been proposed that vacant pockets in proteins could accommodate non-valence states⁶¹. Proteins and enzymes play a crucial role in almost all biological reactions, particularly in the transfer and transport of electrons through biological matter. These processes are central to vital phenomena such as photosynthesis⁶⁷, aerobic respiration⁶⁸, and biological nitrogen fixation⁶⁹. The range of these electron transfers is remarkable, spanning timescales from picoseconds to milliseconds and distances between donor and final acceptor molecules from a few to over hundreds of Ångströms^{70,71}. Long-range electron transport is typically achieved through a chain of cofactors, often metal clusters, which facilitate a stepwise transfer of the electron. The inter-cluster distances range from a few Ångströms to over 20. As an example, in respiratory complex I, NADH donates electrons to reduce ubiquinone⁷². The binding sites of both molecules

are around 110 Å apart, and the electron transfer is mediated by a series of cofactors. To model these transfer reactions, it is commonly assumed that the electron tunnels between the donor and acceptor. Specifically, in the superexchange model, the tunnelling process is mediated by anionic states in the intervening space, effectively lowering the tunnelling barrier⁷¹. The sensitivity of non-valence anion states to environmental factors suggests a potential and elegant mechanism that natural systems could exploit to regulate long-range electron transfer processes.

This study focuses on other biological targets, which could display an interplay between NVSs and VBSs. A natural compound with relevant roles in electron transfer in biological processes is ubiquinone.

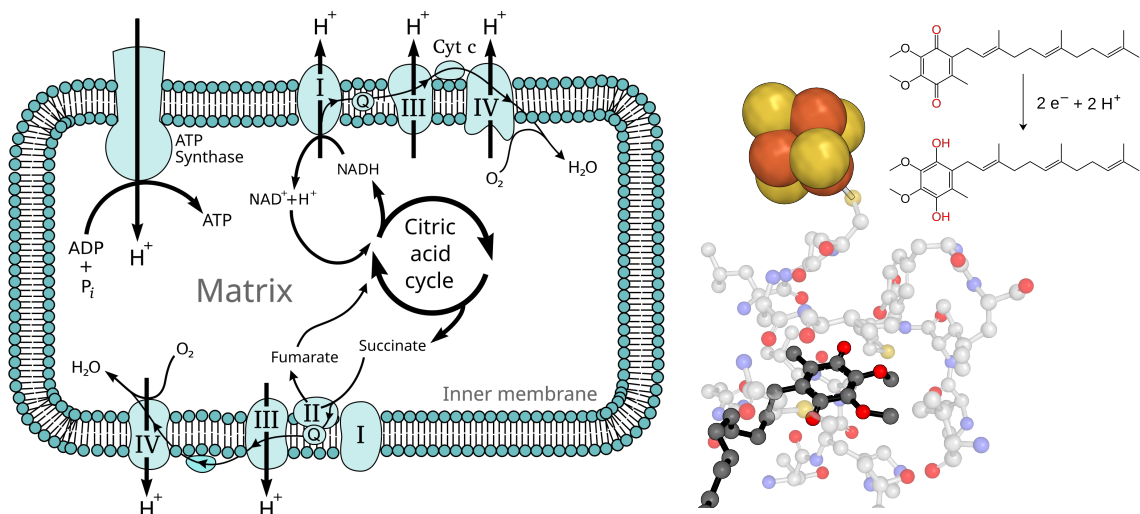


Figure 1.2: Roles of ubiquinone. Left; electron transport chain in the mitochondria, ubiquinones get reduced at complexes I and II and oxidized at complex III, adapted from Ref. 73. Right: CoQ at the active site of bacterial complex I (PDB: 6I0D)⁷⁴ and ubiquinone to ubiquinol interconversion.

1.2 UbiQuinone

Quinones, named for the bark of the cinchona tree from which they were isolated in the 18th century⁷⁵, are a class of organic compounds with a fully conjugated cyclic dione structure derived from aromatic compounds by conversion of an even number of C-H to ketone groups⁷⁶. Quinones are known for their redox properties and play crucial roles in various biological processes, including electron transport in cellular respiration and photosynthesis^{72,77}.

This work focuses on ubiquinone -*ubi* from being ubiquitous in nature-, also known as coenzyme Q (CoQ), a lipid-soluble molecule that can exist as two tautomers: a ketone or alcohol, then named ubiquinol. It plays a role in aerobic respiration in the electron transport chain (ETC) as an electron carrier. As schematised in Figure 1.2, ubiquinone accepts 2 electrons at complexes I or II and donating them in complex III⁷².

Ubiquinone is composed of a benzoquinone ring, 2,3-dimethoxy-6-methyl-p-benzoquinone, and a long side chain, composed of a variable number of isoprenoid units depending on the organism, 10 in humans. This number, n , is used for the naming of the specific ubiquinone (Q_n). In Figure 1.3 different Q_n are presented. The benzoquinone moiety is responsible for its redox properties, while the isoprenoid tail enhances its lipid solubility, allowing it to integrate into biological membranes.⁷²

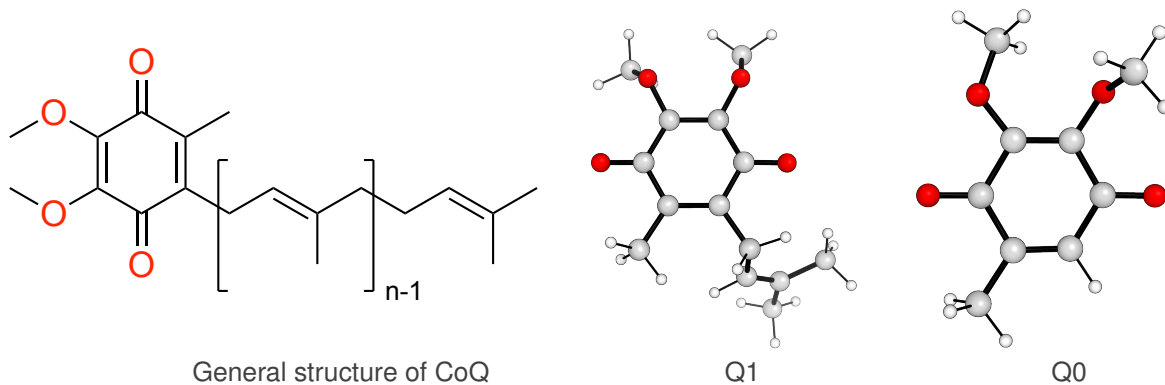


Figure 1.3: Quinones considered in this work. From left to right: General structure of CoQ (or Q_n), Q_1 , Q_0 .

The ubiquinone moiety can support two types of anion states, a VBS and a DBA. In p-benzoquinone, the valence anion can be understood from the Hückel picture with the excess electron occupying a vacant π^* orbital. This state is stabilised relative to benzene due to the electron withdrawing ketone groups. In ubiquinone, the VBS is bound by around 1.7 eV⁷⁷. The dipole-bound anion, on the other hand, results from the two methoxy chains, whose configuration mainly controls the dipole of the molecule⁴¹. It is a fairly rigid molecule, except for the dihedral angles between the methoxy groups and the benzoquinone ring and the isoprenoid tail. Their configuration will affect the dipole moment and could therefore determine the existence and energetics of the DBA^{41,78}. Therefore, fairly complicated electronic structure can be studied in terms of two coordinates.

When the isoprenoid tail is considered, it has been shown that it further stabilises the valence anion⁴². Its effects on the dipole state have not been studied. One can imagine

the effect to be moderate for shorter tails; it will slightly modify the dipole moment of the system, but structurally will be quite far from the excess electron density. For longer tails, the isoprenoid chain could sterically hinder the dipole-bound state.

There have been extensive studies on the electron binding properties of the ubiquinone family, both experimentally^{41,42,78,79} and theoretically^{41,42,48,80,81}. However, these studies have focused on the valence anion of the quinone, and no comprehensive study of the dipole bound state has been performed. The VBS is the final acceptor of the electron and the existence of the DBA in condensed phase is dubious. However, experimental studies have observed dipole-bound anions in the gas phase in ubiquinones Q₀ and Q₁⁴¹. Although its signal is reduced as more isoprenoid units are added, interpreted as an effect of the isoprenoid tail being flexible and resulting in a steric hindrance of the state^{41,42}, one could imagine that in a protein moiety, the geometry of the tail would be fixed far from a potential DB orbital, which could even be further stabilised by residues pointing in the cavity. This motivates the current study.

1.3 Research Goals

The main objective of this work is to theoretically study the dipole-bound anions of ubiquinone. The electron attachment variant of equation-of-motion CC2 (EA-EOM-CC2) is used, which has recently shown to be adequate for dipole bound states of organic molecules⁵¹. The specific objectives are:

- Benchmark the reliability of the EA-EOM-CC2 method to compute the electron affinity of quinones.
- Implement the Dyson orbital approach for EOM-CC2, for characterisation of electronic states of large systems beyond their energies.
- To investigate the dipole-bound anions of ubiquinone in terms of its functional group configurations.
- To study the effect of the molecular environment on the dipole-bound anion of ubiquinone.

Chapter 2

Theoretical Background

2.1 Ground State Electronic Structure Methods

Electronic structure theory aims to solve the time-independent Schrödinger equation (TISE) for a many-electron system, which governs the behavior of electrons within atoms and molecules:

$$\hat{H}\Psi = E\Psi \quad (1)$$

However, solving the TISE exactly for systems with more than one interacting electron is unfeasible due to its many body nature. To address this, approximate methods such as the Hartree-Fock (HF) method have been developed^{82,83}.

The Hartree-Fock (HF) method stands as the cornerstone electronic structure calculations⁸⁴. The HF method provides an approximate solution to the TISE within the Born-Oppenheimer approximation by assuming that each electron moves independently within an average electrostatic field generated by the other electrons in the system and nuclei. In the HF method the N -electron wavefunction is represented by a Slater determinant, which is formed by taking the antisymmetrized product of N individual one-electron spin-orbitals (ϕ):

$$\Psi(\mathbf{r}_1, \mathbf{r}_2, \dots, \mathbf{r}_N) = \frac{1}{\sqrt{N!}} \begin{vmatrix} \phi_1(\mathbf{r}_1) & \phi_2(\mathbf{r}_1) & \cdots & \phi_N(\mathbf{r}_1) \\ \phi_1(\mathbf{r}_2) & \phi_2(\mathbf{r}_2) & \cdots & \phi_N(\mathbf{r}_2) \\ \vdots & \vdots & \ddots & \vdots \\ \phi_1(\mathbf{r}_N) & \phi_2(\mathbf{r}_N) & \cdots & \phi_N(\mathbf{r}_N) \end{vmatrix} \quad (2)$$

The choice of using a determinant inherently satisfies the antisymmetry requirement of fermions. The energy expectation for a Slater determinant according to HF is variational

and can be computed as:

$$\begin{aligned}
 E_{HF} &= \langle \Psi | \sum_{i=1}^N \hat{F}_i | \Psi \rangle \\
 &= \langle \Psi | \sum_{i=1}^N \hat{h}(i) + \sum_{i,j=1}^N (2\hat{J}_j(i) - \hat{K}_j(i)) | \Psi \rangle \\
 &= \sum_{i=1}^N \langle \phi_i | \hat{h} | \phi_i \rangle + \frac{1}{2} \sum_{i,j=1}^N \langle \phi_i \phi_j | | \phi_i \phi_j \rangle
 \end{aligned} \tag{3}$$

Where, \hat{F} is the Fock operator. \hat{F} is made up from \hat{h} , the one-electron core Hamiltonian operator (kinetic energy and electron-nucleus attraction); $\hat{J}_j(i)$, the Coulomb operator, describing the electrostatic repulsion between electron i and the average charge distribution of electron j , and $\hat{K}_j(i)$ is the exchange operator, a purely quantum mechanical term arising from the antisymmetry principle. Because the Fock operator depends on the spinorbitals of all the other electrons, their interactions are coupled. Consequently, these equations cannot be solved analytically and are solved using an iterative procedure known as the self-consistent field (SCF) method. Here, the requirement is that the final field experienced by the electrons must be consistent with the electron distribution that generates that field. This procedure is variational under the constraint that the molecular spinorbitals are orthonormal. Due to the two electron repulsion and exchange contributions, HF scales as $\mathcal{O}(N^4)$ in terms of computational cost, where N is the number of spinorbitals in the system.

In practical Hartree-Fock calculations, the spinorbitals are expressed as linear combinations of predefined mathematical functions known as basis functions. The set of these functions is called a basis set. Because a finite basis set cannot exactly represent the spinorbitals, they define the level of accuracy and computational cost of the calculation. Larger basis sets generally lead to more accurate descriptions of the electronic structure at the cost of increased computational effort.

2.1.1 Electron Correlation

The Hartree-Fock (HF) method is inherently limited by its neglect of the instantaneous interactions of electrons. In the HF approximation, each electron is treated as moving independently within a static, average field created by the other electrons. This mean-field approach fails to account for the fact that electrons will instantaneously repel each other, leading to a correlated movement as they try to avoid each other in space.

The primary consequence of neglecting electron correlation in the HF approximation is an overestimation of the electron-electron repulsion energy, known as dynamic correlation. Due to this, the HF electronic energy is higher than the exact energy, and HF wavefunctions fail to capture certain phenomena, such as London dispersion forces or non-valence states.

Correlated methods aim to include the effects of the instantaneous interactions between electrons that are neglected in the mean-field approximation of HF theory. In the following sections, several correlated methods relevant to this work are presented.

2.1.2 Møller-Plesset Perturbation Theory

Møller-Plesset (MP)⁸⁵ perturbation theory offers a way to improve upon the HF energy by the use of Rayleigh-Schrodinger perturbation theory: the electron correlation is treated as a perturbation to the HF Hamiltonian. The energy and wavefunction are then expanded as a series in terms of the perturbation strength. The first-order energy correction in MP theory is zero, so the first non-trivial correction to the HF energy appears at the second order, giving rise to the MP2 method. The MP2 energy correction for a closed-shell molecule is given by:

$$E_{\text{MP2}} = -\frac{1}{4} \sum_{ij}^{\text{occ}} \sum_{ab}^{\text{virt}} \frac{|\langle \phi_i \phi_j | \phi_a \phi_b \rangle|^2}{\epsilon_a + \epsilon_b - \epsilon_i - \epsilon_j} \quad (4)$$

Where i, j denote occupied molecular orbitals, a, b denote virtual molecular orbitals, and ϵ are the corresponding orbital energies from the HF calculation. MP theory can be extended to higher orders (MP3, MP4, etc.) to achieve greater accuracy, although the computational cost increases significantly with each order. The computational cost of MP2 scales as $\mathcal{O}(N^5)$. This approximation captures same spin and opposite spin electron pair correlation at different levels of accuracy. To fix this imbalance, additional corrections have been developed without increasing the computational cost. Spin-component scaling (SCS)⁸⁶ is a technique where empirical scaling factors are applied to the correlation energies of same-spin (c_{ss}) and opposite-spin (c_{os}) electron pairs.

2.1.3 Density Functional Theory

Density functional theory (DFT)^{87,88} provides an alternative approach to incorporating electron correlation by parametrizing the energy on the electron density rather than the wavefunction, reducing the degrees of freedom of a system composed by N electrons from $3N - 3$ to just 3. In the most commonly used form of DFT, the Kohn-Sham method,

the problem is formulated in terms of orbitals that are not physical, but are chosen to reproduce the electron density of the system. This enables the problem to be treated analogously to HF theory and solved using the SCF procedure. The fundamental principle of DFT is that the ground state energy of a system is a unique functional of its electron density:

$$\left(-\frac{1}{2}\nabla^2 + \hat{V}_{\text{ext}}(\mathbf{r}) + \hat{V}_{\text{H}}(\mathbf{r}) + \hat{V}_{\text{XC}}[\rho(\mathbf{r})] \right) \phi_i(\mathbf{r}) = \epsilon_i \phi_i(\mathbf{r}) \quad (5)$$

where $\rho(\mathbf{r})$ is the electron density, \hat{V}_{ext} denotes the external potential, and $\hat{V}_{\text{H}}(\mathbf{r}) = \int \frac{\rho(\mathbf{r}')}{|\mathbf{r}-\mathbf{r}'|} d\mathbf{r}'$ is the Hartree potential, which describes the electrostatic interaction of the electron density with both the nuclei and itself. \hat{V}_{XC} is the exchange-correlation potential, designed to account for electron correlation effects. The exact form of the exchange-correlation functional is unknown and must be approximated; consequently, the accuracy of DFT calculations is highly dependent on the choice of functional. The computational cost of DFT scales as $\mathcal{O}(N^4)$, although in some implementations this can be reduced down to $\mathcal{O}(N \log N)$ by employing techniques such as the fast multipole method.

2.1.4 Configuration Interaction

Configuration Interaction (CI)^{85,89} methods improve upon HF by expressing the electronic wavefunction as a linear combination of the HF ground state determinant and excited determinants:

$$|\Psi_{\text{CI}}\rangle = c_0 |\Psi_0\rangle + \sum_{ia} c_{ia} |\Psi_{ia}\rangle + \sum_{ijab} c_{ijab} |\Psi_{ijab}\rangle + \dots \quad (6)$$

Where $|\Phi_0\rangle$ is the HF ground state determinant, $|\Psi_{ia}\rangle$ represents a determinant with a hole in spin-orbital i and a particle in the spin-orbital a , and c are the CI coefficients. Full CI includes all possible excitations within a given one-electron basis set and represents the exact solution to the non-relativistic Schrödinger equation in that basis. However, is computationally prohibitive for all but the simplest systems and in practice CI methods are always truncated to a small number of excitations.

Truncated CI methods, such as CISD (singles and doubles), are more practical but lack size extensivity and size consistency, making them unsuitable for extensive methods. Size extensivity⁹⁰ requires that the energy of a system scales linearly with the number of electrons, while size consistency⁹¹ requires that the energy of a system with no interaction between its subsystems is equal to the sum of the energies of the individual subsystems.

2.1.5 Coupled Cluster Theory

Similarly to CI, the coupled cluster (CC)^{85,92–95} method expands the wavefunction as a linear combination of Slater determinants. However, the CC wavefunction is size-extensive and size-consistent by using an exponential ansatz,

$$|\Psi_{\text{CC}}\rangle = e^{\hat{T}}|\Psi_0\rangle \quad (7)$$

where \hat{T} is the cluster operator, which is the central component of CC theory and is defined as a sum of excitation operators,

$$\hat{T} = \hat{T}_1 + \hat{T}_2 + \hat{T}_3 + \cdots + \hat{T}_N \quad (8)$$

where N is the total number of electrons in the system. Each term in this sum corresponds to a specific level of excitation and is expressed within the second quantization formalism as:

- $\hat{T}_1 = \sum_i^{\text{occ}} \sum_a^{\text{virt}} t_i^a a_a^\dagger a_i$ represents single excitations.
- $\hat{T}_2 = \frac{1}{4} \sum_{i,j}^{\text{occ}} \sum_{a,b}^{\text{virt}} t_{ij}^{ab} a_a^\dagger a_b^\dagger a_j a_i$ represents double connected, or *coupled*, excitations.
- Higher-order excitation operators $\hat{T}_3, \hat{T}_4, \dots$ describe connected excitation of three, four, and more electrons, respectively.

The coefficients t_i^a , t_{ij}^{ab} , etc., are cluster amplitudes determined by projection of the Schrödinger equation onto each excited determinant Ψ_{exc} :

$$0 = \langle \Psi_{\text{exc}} | e^{-\hat{T}} \hat{H} e^{\hat{T}} | \Psi_0 \rangle \quad (9)$$

creating a non-linear equation system that is solved iteratively. The energy is obtained by projecting the Schrödinger equation onto the HF reference determinant:

$$E_{\text{CC}} = \langle \Psi_0 | e^{-\hat{T}} \hat{H} e^{\hat{T}} | \Psi_0 \rangle \quad (10)$$

The exponential form expanded as a Taylor series, $e^{\hat{T}} = 1 + \hat{T} + \frac{1}{2!} \hat{T}^2 + \dots$, inherently includes terms that represent disconnected clusters, which ensures size consistency. It can be shown that the exponential operators in Eq. 10 can be simplified to a series of commutators which ends at the fourth order. The cluster operator \hat{T} can be truncated at different levels of excitation:

- **CCD** (Coupled Cluster Doubles): This is the simplest approximation in the CC family, where the cluster operator is truncated to include only double excitations: $\hat{T} = \hat{T}_2$.

- **CCSD** (Coupled Cluster Singles and Doubles): This is one of the most widely used and generally accurate *ab initio* methods, where the cluster operator includes both single and double excitations: $\hat{T} = \hat{T}_1 + \hat{T}_2$.
- **CCSDT** (Coupled Cluster Singles, Doubles, and Triples): $\hat{T} = \hat{T}_1 + \hat{T}_2 + \hat{T}_3$.
- ...

The hierarchy can be extended to include even higher levels of excitation, with the properties converging to the FCI limit. CCSD is a highly accurate method that is able to capture most of the dynamic correlation and CCSD(T), where the triple excitations are treated perturbatively, is considered the gold standard in computational chemistry. The computational cost of CC methods increases rapidly with the level of truncation, as shown in Table 2.1.

Because of the truncation of the excitation operators, the similarity-transformed Hamiltonian, $e^{-T}\hat{H}e^T$, becomes non-Hermitian, leading to distinct left and right eigenfunctions for the same eigenvalue that form a biorthonormal set, satisfying $\langle\Psi_i^L|\Psi_j^R\rangle = \delta_{ij}$. While the right eigenfunction is parametrised as $|\Psi_{CC}\rangle = e^{\hat{T}}|\Phi_0\rangle$, the left eigenfunction is expressed as $\langle\Psi_{CC}^L| = \langle\Phi_0|(1 + \hat{\Lambda})e^{-\hat{T}}$, where $\hat{\Lambda}$ is the de-excitation operator:

$$\hat{\Lambda} = \hat{\Lambda}_1 + \hat{\Lambda}_2 + \dots = \sum_i^{\text{occ}} \sum_a^{\text{virt}} \lambda_a^i a_i^\dagger a_a + \frac{1}{4} \sum_{ij}^{\text{occ}} \sum_{ab}^{\text{virt}} \lambda_{ab}^{ij} a_i^\dagger a_j^\dagger a_b a_a + \dots \quad (11)$$

and λ the amplitudes to be determined in an equivalent manner to the t amplitudes:

$$\langle\Psi_0|(1 + \hat{\Lambda})e^{-\hat{T}}\hat{H}e^{\hat{T}}|\Psi_{exc}\rangle = 0 \quad (12)$$

2.1.6 Second Approximate Coupled Cluster

Second approximate coupled cluster (CC2)^{50,85,96} belongs to the broader family of CCn approximate coupled cluster methods, where the ‘n’ in CCn indicates the truncation of the cluster operator within a perturbative hierarchy. These methods aim to reduce the computational cost associated with standard CC truncations while still retaining a reasonable level of accuracy. In CC2, the energy and single amplitudes are calculated using the same equations as in CCSD (Eq. 7), but the doubles amplitudes are approximated using a non-iterative expression identical to those in MP2 theory:

$$t_{ij}^{ab} = \frac{1}{1 + \delta_{ij}\delta_{ab}} \frac{\langle\phi_a\phi_b||\phi_i\phi_j\rangle}{\epsilon_a + \epsilon_b - \epsilon_i - \epsilon_j} \quad (13)$$

where ϵ are the HF orbital energies, δ_{pq} is the Kronecker delta function, and $\langle ab||ij \rangle$ are the two-electron integrals. While this approximation leads to a less accurate description of electron correlation compared to CCSD, the perturbative treatment of the doubles amplitudes in CC2 reduces the computational cost to $\mathcal{O}(N^5)$. While the ground state CC2 energy is of comparable quality to MP2, the advantage of the former is that a clear response hierarchy for excited states can be defined. The CC2 method is particularly useful when the computational cost of CCSD is prohibitive, such as large systems with many electrons. SCS, with the same scaling factors as MP2, has been shown to improve the accuracy of CC2^{51,86,97}.

Additionally, the memory scaling can be reduced to N^3 by using the resolution-of-the-identity (RI) approximation for the two electron integrals, which are approximated using an auxiliary basis set, reducing each four-index quantity to a product of two three-index quantities⁹⁶.

Table 2.1: Computational scaling of quantum chemistry methods, canonical memory usage is indicated as Memory, whereas RI memory usage is indicated as RI Memory. The operation count is given in terms of the number of spin-orbitals, N .

Method	Operation count	Memory	RI Memory
HF	$\mathcal{O}(N^4)$	$\mathcal{O}(N^4)$	$\mathcal{O}(N^3)$
MP2	$\mathcal{O}(N^5)$	$\mathcal{O}(N^4)$	$\mathcal{O}(N^3)$
KS DFT	$\mathcal{O}(N^4)$	$\mathcal{O}(N^4)$	$\mathcal{O}(N^3)$
CCD/CCSD	$\mathcal{O}(N^6)$	$\mathcal{O}(N^4)$	$\mathcal{O}(N^4)$
CCSDT	$\mathcal{O}(N^8)$	$\mathcal{O}(N^6)$	$\mathcal{O}(N^6)$
CC2	$\mathcal{O}(N^5)$	$\mathcal{O}(N^4)$	$\mathcal{O}(N^3)$

2.2 Equation-of-Motion Methods

Equation-of-motion coupled cluster (EOM-CC) methods^{98–100} are an extension of ground-state coupled cluster theory to excited (EE), ionized (IP) and electron-attached (EA) states. In EOM-CC theory, the target electronic state is generated by applying a linear excitation operator \hat{R} to a reference state, which is the coupled cluster wavefunction of the ground state. The target state wavefunction can then be expressed as $|\Psi_{\text{EOM}}\rangle = \hat{R}|\Psi_{\text{CC}}\rangle = \hat{R}e^{\hat{T}}|\Phi_0\rangle$. Figure 2.1, shows some of the determinants of $|\Psi_{\text{EA}}\rangle$, the EOM flavour relevant to this work, where the target state has one more α -spin electron.

The form of the operator \hat{R} is similar to the cluster operator and chosen to access the

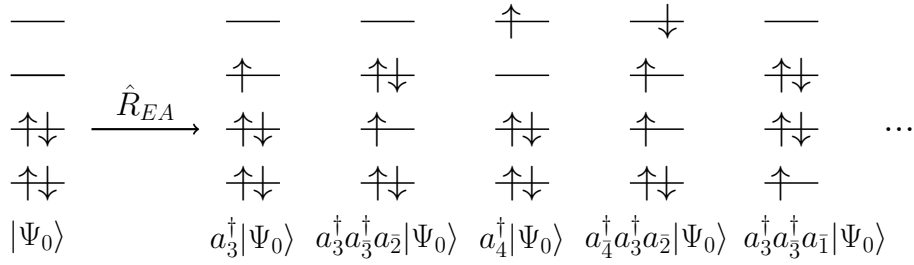


Figure 2.1: Schematic representation of the EOM-EA method. The target state is generated by applying the electron attachment operator \hat{R}^{EA} to the reference state. The resulting wavefunction contains contributions from various determinants with one more α electron.

desired target state. In the case of EOM-EA, the electron attachment operator R^{EA} includes terms that describe the creation of one electron in an unoccupied orbital, terms that describe the creation of one electron accompanied by the excitation of another electron:

$$\hat{R}^{\text{EA}} = \hat{R}_1^{\text{EA}} + \hat{R}_2^{\text{EA}} + \dots = \sum_a r^a a_a^\dagger + \frac{1}{2} \sum_{ab} \sum_i r_i^{ab} a_a^\dagger a_b^\dagger a_i + \dots \quad (14)$$

where a and b denote virtual orbitals, i denotes an occupied orbital, and r^a and r_i^{ab} are the coefficients to be determined. By truncating \hat{R} at the same excitation level as the cluster operator, the method is rigorously size-extensive and size-consistent. The EA energies, or any other EOM energy, can be obtained as the eigenvalues of the similarity-transformed Hamiltonian, \bar{H}_{N} :

$$\bar{H}_{\text{N}} \hat{R} |\Psi_0\rangle = \Delta E_{\text{EOM}} \hat{R} |\Psi_0\rangle \quad (15)$$

$$\bar{H}_{\text{N}} = e^{-\hat{T}} \hat{H} e^{\hat{T}} - \langle \Psi_0 | e^{-\hat{T}} \hat{H} e^{\hat{T}} | \Psi_0 \rangle \quad (16)$$

As in coupled cluster, the similarity transformed Hamiltonian is non-Hermitian and left and right eigenvectors are different but correspond to the same eigenvalues. This means that the properties have ‘right’ and ‘left’ transition moments. The left deexcitation operator \hat{L} , analogous to \hat{R} for the left eigenstates, takes the following form for EOM-EA:

$$\hat{L}^{\text{EA}} = \hat{L}_1^{\text{EA}} + \hat{L}_2^{\text{EA}} + \dots = \sum_a l^a a_a + \frac{1}{2} \sum_{ab} \sum_i l_{ab}^i a_i^\dagger a_b a_a + \dots \quad (17)$$

Where l_a and l_{ba}^i are the amplitudes to be determined. And the ‘left’ wavefunction is $\langle \Psi_{\text{EOM}} | = \langle \Psi_{\text{CC}} | \hat{L} = \langle \Phi_0 | \hat{L} e^{-\hat{T}}$.

One strength of the EOM-CC ansatz is the ability to use of a closed shell reference to access open shell states, which are eigenfunctions of the \hat{S}^2 operator. Finally, in the case relevant to this work, the computational cost of the EOM component in EA-EOM-CC

methods scales as $\mathcal{O}(N^5)$, thus rendering the CC reference the computational bottleneck. This is still true in the case of CC2, which also scales as $\mathcal{O}(N^5)$, since its expression contains more nonlinear terms.

2.3 Dyson Orbitals

Dyson orbitals^{101,102} are defined as the overlap between the wavefunction of an initial N -electron state ($|\Psi_0^N\rangle$) and the wavefunction of the final state with $N \pm 1$ electrons ($|\Psi_f^{N+1}\rangle$).

$$\phi_d(r_1) = \sqrt{N} \int \Psi^N(r_1, \dots, r_{N-1}) \Psi^{N+1}(r_1, r_2, \dots, r_N) dr_1 \dots dr_{N-1} \quad (18)$$

Because the terms differ in one electron, the result of the overlap is a scalar field, which is a vector in the Hilbert space, expressed as a linear combination of the molecular orbitals ($\phi_p(r)$) of the reference wavefunction:

$$\phi_d(r) = \sum_p \gamma_p \phi_p(r) \quad (19)$$

where γ_p are the coefficients that quantify the contribution of each molecular orbital to the Dyson orbital. Physically, Dyson orbitals can be interpreted as the correlated analogue to the orbital of the electron that is either removed or attached. The squared norm of the Dyson orbital, P , is calculated by integrating over all space:

$$P = \int |\phi_d(r)|^2 dr = \sum_{p,q} \gamma_p^* \gamma_q \langle \phi_p | \phi_q \rangle \quad (20)$$

It ranges from 0 to 1 and provides a direct measure of the one-electron character of the ionization or electron attachment process. If the open shell wavefunction is obtained by means of an EOM-CC method, there is a ‘left’ and a ‘right’ Dyson orbital. By convention, the right Dyson orbital is obtained when Ψ^{N+1} is in the bra and Ψ^N is in the ket.

On top of providing a visual representation of the ionization or electron attachment process, they can be used for the interpretation and prediction of photoelectron spectra as they contain all the information required to calculate differential cross-sections, $\frac{d\sigma}{d\Omega_k}$:

$$\frac{d\sigma}{d\Omega_k} = \frac{4\pi^2 k E}{c} |\langle \phi_d | \mu | \Psi_k^{el} \rangle|^2 \quad (21)$$

where k is the magnitude of the photoelectron wavevector, E is the energy of the ionizing

radiation, and c is the speed of light, μ is the dipole operator, and Ψ_k^{el} is the photoelectron wavefunction, and strong orthonormality is assumed between the reference and continuum wavefunction.

2.3.1 EOM-CC2 Dyson Orbital Equations

The algebraic expressions for the EOM-CC2 Dyson orbitals are identical to the CCSD ones. A derivation of the algebraic expression of Dyson orbitals in terms of the t , r , l , λ amplitudes is presented for the EA-EOM case, and the expression for the other EOM flavours implemented in this work are provided.

It is important to realize that the operators involved ($\hat{T}, \hat{\Lambda}, \hat{R}, \hat{L}$) affect the occupation of the spin-orbitals, and thus only the combinations of terms which leave the reference wavefunction, $|0\rangle$, unchanged survive. To find these combinations, commutators can be used to reorder the operators involved. To simplify the equations involved, a change of notation is introduced: $|\Psi_{CC}\rangle \equiv |CC\rangle$ and $|\Psi_{EOM}\rangle \equiv |EOM\rangle$.

EOM-EA-CC Dyson Equations

In the case of the right EOM-EA-CC Dyson orbital amplitudes:

$$\gamma_i^{\text{EA,R}} = \langle EA | \hat{a}_i^\dagger | CC \rangle = \langle 0 | \hat{L}^{\text{EA}} e^{-\hat{T}} \hat{a}_i^\dagger e^{\hat{T}} | 0 \rangle$$

The following equalities are useful:

$$e^{-\hat{T}} e^{\hat{T}} = e^{\hat{T}} e^{-\hat{T}} = 1$$

$$[e^{\pm\hat{T}}, \hat{a}_p^\dagger] = \cancel{[1, \hat{p}^\dagger]}^0 \pm \sum_{bj} t_j^b [\hat{b}^\dagger \hat{j}, \hat{p}^\dagger] + \sum_{bcjk} \frac{1}{2} t_{jk}^{bc} [\hat{b}^\dagger \hat{c}^\dagger \hat{j} \hat{k}, \hat{p}^\dagger] + \dots$$

where a change of notation, $a_p^\dagger \rightarrow p^\dagger$, upon expansion is done for readability. Two cases are distinguished, p is a virtual orbital, a , or an occupied orbital, i . For virtual orbitals, $p = a$:

$$[\hat{b}^\dagger \hat{j}, \hat{a}^\dagger] = \hat{b}^\dagger \hat{j} \hat{a}^\dagger - \hat{a}^\dagger \hat{b}^\dagger \hat{j} = (-1)^2 \hat{a}^\dagger \hat{b}^\dagger \hat{j} - \hat{a}^\dagger \hat{b}^\dagger \hat{j} = 0$$

Similarly with higher order terms, one arrives at:

$$[e^{\pm\hat{T}}, \hat{a}_a^\dagger] = 0$$

For occupied orbitals, $p = i$:

$$[\hat{b}^\dagger \hat{j}, \hat{i}^\dagger] = \hat{b}^\dagger \hat{j} \hat{i}^\dagger \cancel{^0} - \hat{i}^\dagger \hat{b}^\dagger \hat{j}$$

And similarly with higher order terms:

$$[e^{\pm\hat{T}}, \hat{a}_i^\dagger] = -\hat{a}_i^\dagger(e^{\pm\hat{T}} - 1)$$

These relations can now be used to derive the expression for the occupied and virtual right EOM-EA-CC Dyson orbital amplitudes:

$$\phi_D^{EA,R} = \sum_p \gamma_p^{EA,R} \phi_p = \sum_i^{\text{occ}} \gamma_i^{EA,R} \phi_i + \sum_a^{\text{vir}} \gamma_a^{EA,R} \phi_a$$

The general expression can be reordered:

$$\begin{aligned} \gamma_p^{EA,R} &= \langle EA | \hat{a}_p^\dagger | CC \rangle = \langle 0 | \hat{L}^{EA} e^{-\hat{T}} \hat{a}_p^\dagger e^{\hat{T}} | 0 \rangle \\ &= \langle 0 | \hat{L}^{EA} (\hat{a}_p^\dagger e^{-\hat{T}} + [e^{-\hat{T}}, \hat{a}_p^\dagger]) e^{\hat{T}} | 0 \rangle \end{aligned} \quad (22)$$

For virtual orbitals, $p = a$:

$$\begin{aligned} \gamma_a^{EA,R} &= \langle 0 | \hat{L}^{EA} (\hat{a}_a^\dagger e^{-\hat{T}} + [e^{-\hat{T}}, \hat{a}_a^\dagger]) e^{\hat{T}} | 0 \rangle \\ &\stackrel{1}{=} \langle 0 | \hat{L}^{EA} \hat{a}_a^\dagger e^{-\hat{T}} e^{\hat{T}} | 0 \rangle = \langle 0 | \hat{L}^{EA} \hat{a}_a^\dagger | 0 \rangle \\ &= \langle 0 | l_a \hat{a} \hat{a}^\dagger | 0 \rangle \\ &= l_a \end{aligned} \quad (23)$$

For occupied orbitals, $p = i$:

$$\begin{aligned} \gamma_i^{EA,R} &= \langle 0 | \hat{L}^{EA} (\hat{a}_i^\dagger e^{-\hat{T}} + [e^{-\hat{T}}, \hat{a}_i^\dagger]) e^{\hat{T}} | 0 \rangle \\ &\stackrel{0}{=} \langle 0 | \hat{L}^{EA} (\hat{a}_i^\dagger e^{-\hat{T}} - \hat{a}_i^\dagger e^{-\hat{T}} + \hat{a}^\dagger) e^{\hat{T}} | 0 \rangle = \langle 0 | \hat{L}^{EA} \hat{a}_i^\dagger e^{\hat{T}} | 0 \rangle \\ &= \langle 0 | \sum_b l_b t_i^b \hat{b} \hat{i}^\dagger \hat{b}^\dagger \hat{i} + \frac{1}{2} \sum_{jbc} l_{bc}^j t_{ij}^{bc} \hat{b} \hat{c} \hat{j}^\dagger \hat{i}^\dagger \hat{b}^\dagger \hat{c}^\dagger \hat{i} \hat{j} | 0 \rangle \\ &= - \sum_b t_{ib} l_b - \frac{1}{2} \sum_{jbc} t_{ji}^{bc} l_{bc}^k \end{aligned} \quad (24)$$

A similar approach can be applied to the other Dyson equations to obtain their corresponding expressions, which can be found in appendix A.

Chapter 3

Computational Details

All files pertinent to this research are accessible via the [GitHub](#) repository. Electronic structure calculations were conducted using a developer's version of the *Q-Chem* software package¹⁰³. The frozen-core approximation was employed in all calculations, meaning only valence electrons were correlated. Furthermore, the resolution of the identity (RI) approximation was utilised throughout⁹⁶.

3.1 Performance Evaluation of EOM-CC2 Methods

3.1.1 Basis Set Dependence of EA-EOM-CC2 for Dipole-Bound Anions

The influence of the basis set on EA-EOM-CC2 calculations was investigated using a dataset of 14 molecules exhibiting radical dipole-bound anions, as detailed in Ref. 51. These molecules were chosen to represent a broad spectrum of dipole moments and polarisabilities. The calculations employed modified aug-cc-pV_XZ basis sets¹⁰⁴, with the cardinality X ranging from double to quadruple. To accurately describe non-valence states, supplementary diffuse functions were incorporated. A basis set denoted as aug-ccpV_XZ+(2n)s(n)p signifies the addition of 2n s-type and n p-type shells to heavy atoms, and n of each to hydrogen atoms. The exponents for these extra functions were generated by systematically halving the exponent of the most diffuse s and p functions in an even-tempered fashion.

3.1.2 Assessment of EA-EOM-CC2 for Valence-Bound Radical Anion States in Quinones

The efficacy of EA-EOM-CC2 for treating valence-bound radical anion states of quinones was evaluated using a set of 10 molecules previously established in Ref. 49. The molecular geometries corresponded to the optimised structures of the neutral species, which the original authors had optimised at the TPSS/ma-def2-TZVP level of theory. For the spin-component scaling (SCS) points, the factors applied were ($c_{ss}=1/3$) for same-spin and ($c_{os}=6/5$) for opposite-spin contributions, following previous works^{51,86,97}.

3.1.3 Photoelectron Cross-sections from EOM-CC2 and EOM-CCSD

Dyson orbitals for the EOM-CC2 variants, as outlined in Section 2.3.1 and appendix A, were implemented as described. These will be made available in a forthcoming release of *Q-Chem*.

To ascertain the quality of the EOM-CC2 Dyson orbitals, photoelectron cross-sections were computed using the *ezDyson* software^{105,106}. This analysis involved a set of 20 transitions, which were then compared against results obtained from EOM-CCSD Dyson orbitals and the predominant HF orbital within the EOM-CCSD Dyson orbital. The test set comprised the standard *ezDyson* benchmark set from Ref. 106, augmented with 4 photodetachment transitions from dipole-bound anions and 7 photodetachment transitions from valence-bound anions. Graphical representations of these results are provided in appendix B.

3.2 Ubiquinone Computational Models

3.2.1 Potential Energy Surfaces of Quinone Models

A systematic grid scan of the dihedral angles of the methoxy chains in Q_0 and Q_1 was performed in 20° increments. At each grid point, the molecular structure was optimised while constraining the relevant dihedral angles of the methoxy chains (and the isoprene tail for Q_1) using the method of Lagrange multipliers. The angle and dihedral of the isoprene tail relative to the benzene ring were maintained at 114.1° and 111.8° , respectively, values derived from the crystal structure of Complex I (PDB: 6i0d)⁷⁴. All optimised structures are available in the [GitHub repository](#). Geometry optimisations utilised the TPSS functional¹⁰⁷ combined with Grimme's D3BJ pairwise dispersion correction (employing Becke-Johnson damping)¹⁰⁸, and the minimally augmented ma-def2-TZVP basis

set^{109,110}. This level of theory has previously demonstrated good performance for quinone systems⁴⁹.

The resultant geometries served as the basis for subsequent EOM-EA calculations. The reference wavefunction for these calculations was the RHF solution for the ground state of the neutral molecule. Unless otherwise specified, these calculations were performed with the aug-cc-pVDZ+6s3p basis set (*vide supra*) to ensure an adequate description of non-valence states.

For the Dyson orbital computations, only right Dyson orbitals were calculated. This approach expedited the calculations by obviating the need to determine the lambda amplitudes.

3.2.2 Interaction Scans with Small Molecules

Cluster models were constructed based on the Q_0 structure with dihedral angles $\psi = 160^\circ$ and $\phi = -80^\circ$. For interactions with dipolar molecules (all second-row hydrides), the hydride was positioned along the dipole moment vector of the quinone, originating from the Q_0 centre of mass. The dipole moments of the quinone and hydride were then aligned in either parallel or antiparallel orientations. The interaction distance was defined as the separation between the centre of mass of the quinone and the heavy atom of the hydride. In the case of the noble gas cage, the centre of mass of Q_0 was coincident with the centre of the icosahedron. The geometries of these generated systems were not subjected to further optimisation. All geometries, along with the Python scripts used for their generation, are available in the [GitHub repository](#).

Chapter 4

Results and Discussion

4.1 Performance of EOM-CC2 Methods

This section examines the performance of the EA-EOM-CC2 method for calculating electron affinities. Previous work has shown that EA-EOM-CC2 performs adequately for dipole-bound states (DBSs), whilst tending to overestimate vertical electron affinities (VEAs) for valence-bound states (VBSs)⁵¹. The following analysis focuses on three aspects: the basis set dependence for DBSs in section 4.1.1, the method’s performance for VBSs using a test set of quinones in section 4.1.2, and the efficacy of CC2 in generating Dyson orbitals through comparison of photodetachment cross-sections calculated with EOM-CC2, EOM-CCSD and HF in section 4.1.3.

4.1.1 Basis Set Dependence of EA-EOM-CC2 in Dipole Bound Anions

The basis set dependence of EA-EOM-CC2 for dipole-bound radical anions was evaluated using a test set of 14 DBS of organic molecules taking as reference EA-EOM-CCSD⁵¹. The results as summarised in Table 4.1. The binding energies range from less than 1 meV for acetone to approximately 26 meV for nitrobenzene. The table also shows how the binding energy does not correlate strongly with the magnitude of the dipole moment for different species. For instance, phenylisocyanide, which has a slightly lower dipole moment than benzaldehyde, exhibits an electron affinity nearly twice as large.

The basis set cardinality was varied from DZ to QZ for EA-EOM-CC2 and from DZ to TZ for CCSD, while keeping additional diffuse functions fixed at 6s3p, *vide infra*, for heavy atoms and 3s for hydrogens, referred to as (6s3p). For the EA-EOM-CC2 method, the influence of diffuse functions was further explored by fixing the cardinality to TZ and incrementally increasing the number of diffuse functions from 2s1p for heavy atoms and

1s for hydrogens, referred to as (2s1p), to 8s4p for heavy atoms and 4s for hydrogens, referred to as (8s4p). The exponents of the diffuse functions are detailed in the methods' section 3.1.1. For comparison, the dipole strength, calculated at the HF level, and Koopmans' theorem (KT), which estimates the binding energy using the energy of the lowest unoccupied molecular orbital, are also included.

Starting with the simplest approximation, KT predicts that all anions with an EOM-EA-CCSD binding energy below 10 meV are unbound. However, even for more strongly bound cases, Koopmans' theorem significantly underestimates the binding energy, capturing only 20% of the binding energy for nitrobenzene, for example.

No DBS is found when only the 2s1p diffuse function are added. At the 6s3p level the DBS energy is converged with respect to the extra diffuse functions added to the basis set, deviating by less than 1 meV from the value obtained with the 8s4p diffuse function. The errors are more pronounced for smaller molecules, such as acetaldehyde and acetone. This could be attributed to the inability of functions centred on a few atoms to adequately cover the spatial extent of the DBS orbital. This reasoning may also explain why the DBS of acetaldehyde is only predicted by RI-EA-EOM-CC2/aug-cc-pVTZ+8s4p, as it employs the most diffuse functions. At the RI-EA-EOM-CCSD/aug-cc-pVTZ+8s4p, the DBS of acetaldehyde is found to be 0.84 meV, compared to the 0.76 meV of CC2.

The binding energy increases with higher cardinality, as expected, due to the increased flexibility of the basis set. However, this effect is less significant than the addition of diffuse functions. For instance, the difference between RI-EA-EOM-CCSD/aug-cc-pVDZ+6s3p and RI-EA-EOM-CCSD/aug-cc-pVTZ+6s3p is less than 1 meV for most cases. Smaller molecules with lower-energy DBSs tend to be more challenging; for example, a TZ basis is required to predict the DBS of acetone. In general, and especially for larger systems, the inclusion of diffuse functions is more critical than the cardinality of the basis set for dipole-bound anions.

CC2/aug-cc-pVTZ+6s3p consistently overestimates the binding energies across all molecules when compared to CCSD/aug-cc-pVTZ+6s3p. The mean absolute error (MAE) is 2.8 meV, with deviations reaching up to 10 meV for nitrobenzene. For this reason, using a smaller cardinality results in a cancellation of errors for CC2. The aug-cc-pVDZ+6s3p basis set, when employed with CC2, yields the lowest MAE of 2.3 meV compared to the reference results.

Table 4.1: Electron affinity of dipole-bound radical anions computed using different augmented Dunning basis sets and EOM-EA RI-CC2 and EOM-EA RI-CCSD⁵¹. Koopman' theorem (KT), and dipole moment, μ , calculated at the HF/aug-cc-pVTZ+6s3p level, and mean absolute error (MAE) taking CCSD/aug-cc-pVTZ+6s3p as reference are also given. The values are in meV and Debye respectively.

Molecule		RI-CC2						RI-CCSD			
		aug-cc-pVTZ				pVDZ	pVQZ	pVDZ	pVTZ	KT	μ
		2s1p	4s2p	6s3p	8s4p	6s3p	6s3p	6s3p	6s3p		
Acetaldehyde	CH ₃ CHO	-156.7	-27.8	-3.2	0.8	-4.6	-3.2	-4.6	-3.1	-0.4	3.29
Acetone	(CH ₃) ₂ CO	-114.9	-16.8	1.3	3.3	-0.3	0.9	-0.5	0.9	-5.1	3.46
Acetonitrile	CH ₃ CN	-61.2	12.6	19.9	20.1	18.2	20.3	17.1	18.4	4.2	4.29
Benzaldehyde	C ₆ H ₅ CHO	-97.1	-2.1	8.9	9.6	7.4	9.1	3.4	4.6	-4.9	3.77
N,N-Dimethylformamide	(CH ₃) ₂ NCHO	-81.1	5.4	14.1	14.4	13.2	14.4	13.3	13.7	1.9	4.48
DMSO	(CH ₃) ₂ SO	-84.5	4.0	15.4	16.1	14.8	15.5	14.7	14.9	2.1	4.63
Formamide	CH ₃ NO	-92.2	1.1	16.2	17.2	15.1	17.0	15.1	15.9	3.4	4.28
Methylisocyanide	CH ₃ NC	-95.1	-0.5	10.0	10.5	9.5	10.1	8.8	9.0	-1.8	3.59
Nitrobenzene	C ₆ H ₅ NO ₂	-63.6	30.6	34.8	34.8	32.5	—	25.0	25.9	5.4	5.15
Nitromethane	CH ₃ NO ₂	-82.9	5.7	14.2	14.7	13.0	14.7	12.9	13.7	3.5	4.10
Nitrosobenzene	C ₆ H ₅ NO	-125.0	1.0	11.4	—	9.9	—	5.1	6.0	-4.1	3.73
Phenylisocyanide	C ₆ H ₅ NC	-82.7	8.6	16.3	16.5	15.2	16.7	9.0	9.2	-4.9	3.61
Pyridazine	C ₄ H ₄ N ₂	-80.7	20.5	26.3	26.4	25.0	26.7	18.6	19.1	1.7	4.41
Vinylene carbonate	C ₃ H ₂ O ₃	-82.5	20.9	27.2	27.4	26.4	27.7	25.1	25.5	10	5.05
		MAE	105.3	8.8	2.8	3.4	2.3	2.4	0.8	0.0	12.0

4.1.2 Performance of EA-EOM-CC2 on Valence Bound Radical Anion States of Quinones

Table 4.2: EA-EOM-CC2 benchmark for quinone VBS. Reference values from literature⁴⁹ include experimental adiabatic EAs and vertical EA CCSD(T) calculations using aug-cc-pVDZ basis set with LPNO-CCSD extrapolation to higher cardinal numbers. The RI-CC2 calculations employed three basis sets: aug-cc-pVTZ+6s3p (abbreviated as VTZ+) built as described in section 3.1.1, standard aug-cc-pVTZ (VTZ), and aug-cc-pVDZ (VDZ).

Molecule	#	Exp.	Ref. ⁴⁹	RI-CC2			
			CCSD(T)	SCS		No SCS	
			+E _{CBS}	VTZ+	VTZ+	VTZ	VDZ
Benzoq.	1	1.91	1.64	1.54	2.02	2.02	1.81
Methylbenzoq.	2	1.85	1.57	—	1.95	1.95	1.74
2,5-Dimethylbenzoq.	3	1.76	1.49	1.39	1.89	1.89	1.68
2,6-Dimethylbenzoq.	4	1.77	1.50	1.40	1.89	1.89	1.68
Trimethylbenzoq.	5	1.69	1.43	1.34	1.84	1.84	1.63
Duroq.	6	1.62	1.42	1.32	1.83	1.83	1.62
2,6-Dimethoxybenzoq.	7	1.72	1.32	1.17	1.65	1.65	1.43
Ubiq. (Q_0)	8	1.86	1.50	1.39	1.88	1.88	1.66
Naphthoq.	9	1.81	1.55	—	1.97	1.97	1.76
2-Methylnaphthoq.	10	1.74	1.51	1.45	1.92	1.91	1.71

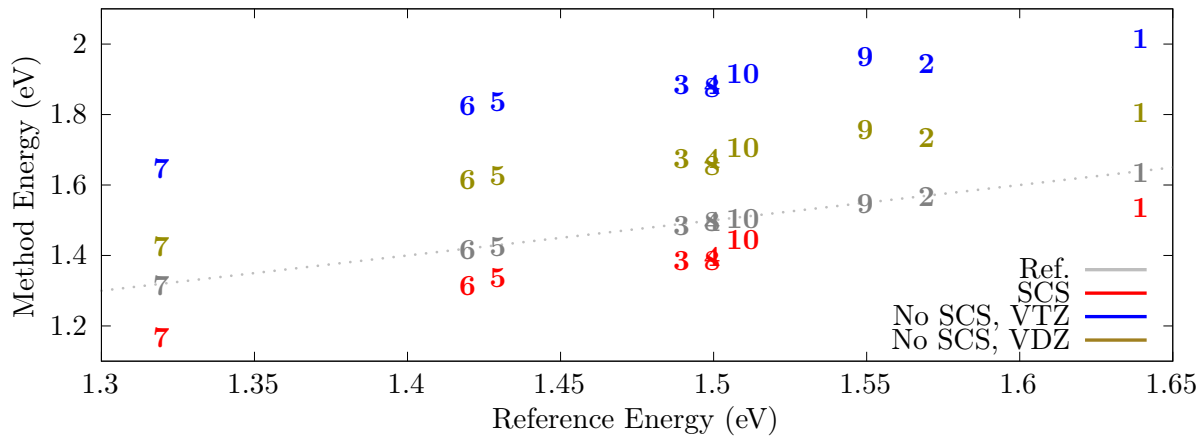


Figure 4.1: Graphical comparison of RI-CC2 methods for quinones. Each point is represented by the compound number given in Table 4.2. The dashed line indicates the reference CCSD(T)+E_{CBS} values.

The performance of EA-EOM-CC2 in calculating the VBS of quinones is benchmarked using a previously established test set of 10 quinones⁴⁹. The results are summarised in Table 4.2 and Figure 4.1. The table includes experimental adiabatic electron affinities

and theoretical CCSD(T)+E_{CBS} reference values.

Previous studies have demonstrated that CC2 typically performs poorly for VBSs; however, the implementation of spin-component scaling (SCS) corrections markedly enhances the accuracy of CC2 for these states⁵¹. The RI-CC2 results presented here include calculations both with and without SCS corrections, utilising two different basis sets: VTZ (aug-cc-pVTZ) and VDZ (aug-cc-pVDZ).

The incorporation of SCS improves the accuracy of CC2 for valence-bound states, corroborating the findings of Ref. 5197. In general unscaled EA-EOM-RI-CC2 overbinds the electron, and the inclusion of SCS results in a slight underbinding. When comparing the results to experimental data, CC2 might appear to provide better agreement than CCSD. This apparent discrepancy arises because the experimental measurements represent adiabatic electron affinities, whilst the calculations determine vertical electron affinities.

As with the case of DBSs, a smaller cardinality leads to a cancellation of errors in the CC2 binding energies, resulting in apparently more exact results (though arising from more inaccurate calculations). Regarding the inclusion of the extremely diffuse functions necessary for modelling DBSs, these have no impact on the VBS energy, indicating that such functions do not contribute to the description of the VBS. Of course, it is still necessary to use augmented basis sets to ensure that the VBS is well described, as the electron density of the VBS is more diffuse than that of the neutral molecule.

It is noteworthy, however, that in all cases, the CC2 method reproduces the correct trend, as illustrated in Figure 4.1. The error introduced remains remarkably consistent across different molecules. Subsequent calculations omit SCS, as both DBS and VBS states can be obtained from the same Hamiltonian; one can expect a systematic overbinding of ~ 0.2 eV ensuring consistency in the results. It is also important to note that DBS predictions are known to deteriorate significantly when SCS is applied⁵¹, and therefore it is not a desirable method for this work.

4.1.3 Photoelectron Cross-section from EOM-CC2/CCSD

As a part of this work, Dyson orbitals between EOM-CC2 states have been implemented within the `ccman2` module of the *Q-Chem* software package. To evaluate their quality, one must go beyond mere visual assessment.

Photodetachment cross-sections for 24 valence bound and dipole bound states were

calculated using the *ezDyson* package^{105,106}. These calculations employ orbitals from three different sources: EOM-CC2 Dyson orbitals, EOM-CCSD Dyson orbitals and the dominant Hartree-Fock orbital. The complete results can be found in appendix B. Figure 4.2 shows two representative examples: the valence bound state of azulene and the dipole bound state of nitromethane.

The results demonstrate that EOM-CC2 successfully captures the essential features of the cross-section, appearing nearly identical in the case of nitromethane's dipole-bound state and showing only minor deviations for azulene. In contrast, using HF orbitals as approximations for Dyson orbitals fails to reproduce the shape obtained with EOM-CCSD. Although a single HF orbital typically dominates the Dyson orbital¹¹¹, the contributions from additional electronic configurations introduced by the correlation prove to be significant.

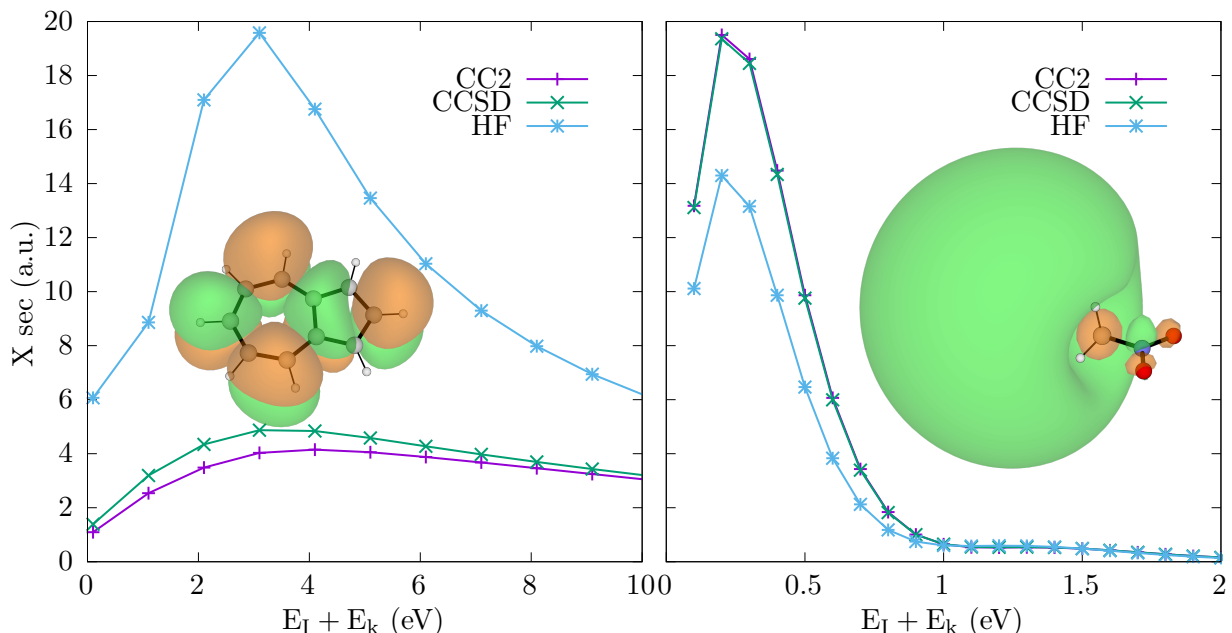


Figure 4.2: Photoedetachment cross-sections of azulene (VBS) and nitromethane (DBS). The cross-sections were calculated using Dyson orbitals from EOM-CC2, EOM-CCSD and the dominant HF orbital in the EOM-CCSD Dyson orbital. The corresponding EA-EOM-CC2 Dyson orbitals are also shown as insets.

4.2 Study on the Anion States of Ubiquinone

Once the performance of the methods has been assessed, the focus shifts to the anion states of ubiquinone (CoQ). All results presented here are based on the calculations performed with RI-EA-EOM-CC/aug-cc-pVDZ+6s3p unless specified otherwise.

4.2.1 Energy and Dipole Surfaces of CoQ

Surfaces of Q0

The conformational landscape of the simplest ubiquinone, Q_0 , was investigated by varying the dihedral angles of the methoxy chains relative to the quinone plane in steps of 20° , as shown in Figure 4.4. These dihedral angles represent the most significant degrees of freedom in the system, as the remainder of the molecule is relatively rigid. This approach enables the construction of potential energy surfaces (PES), dipole strength surfaces, and PES for the anionic states (VBS and DBS), as depicted in Figure 4.3. Owing to the C_2 symmetry present when the methoxy chains are coplanar, only half of the surface points require sampling.

The conformational energy surface of the neutral molecule reveals five minima, corresponding to configurations where the methoxy groups are oriented away from each other. The global minimum occurs at $(180, 180)$, where both chains are coplanar with the quinone and directed oppositely. Four additional minima are found at $(\pm 140, \mp 20)$ and $(\pm 20, \mp 140)$, each approximately 10 meV above the global minimum. The presence of a methyl group at position 5 slightly perturbs the symmetry between the methoxy chains, but its influence on the energy landscape is minimal due to its spatial separation. The energy barriers separating these wells range from 65 to 100 meV, suggesting that interconversion between conformers is feasible at ambient temperature. A pronounced steric repulsion is observed near $(0,0)$, where both methoxy chains are coplanar and oriented towards each other, resulting in an energy penalty of approximately 580 meV.

The dipole strength surface largely reflects the vector sum of the individual methoxy group dipoles. When both chains are aligned in the same direction, the dipole strength is maximised, and vice versa. The lowest dipole moment, below 0.5 Debye, is found near $(180, 180)$. Local maxima in dipole strength are observed at $(0,0)$ with a strength of 2.5 D, and $(\pm 160, \mp 80)$ ($\mu = 3.2$ D), $(\pm 60, \mp 160)$ ($\mu = 3.4$ D), and $(\pm 80, \pm 180)$ ($\mu = 3.2$ D), with the latter two coinciding with conformational minima at $(\pm 140, \mp 20)$.

The valence-bound state (VBS) surface can be rationalised by considering the electron-withdrawing effect of out-of-plane methoxy groups and the electron-donating effect of in-plane conjugation. The VBS minimum is observed at four points where both chains are approximately $\pm 120^\circ$ out of plane, with a vertical electron affinity (VAE) of 1.77 eV. Notably, when either chain is coplanar ($\pm 0^\circ$), the VAE increases by about 0.2 eV. The global minimum occurs at $(0,0)$, where both chains are in-plane, with a VAE of 1.26 eV. The pronounced dependence of the electron affinity on methoxy conformation has been

proposed as a mechanism to control the electron transfer processes in quinone redox enzymes^{49,80,112–114}.

The dipole-bound state (DBS) surface, as anticipated, closely follows the dipole strength surface. It is important to note that in regions where the DBS is unbound, the EA-EOM-CC2 binding energies are not physically meaningful and would approach zero in the basis set limit. Three distinct regions are apparent, mirroring those of the dipole strength surface. The region at ($\pm 60, \pm 180$) ($\mu = 3.1$ D) is the smallest and most weakly bound, with

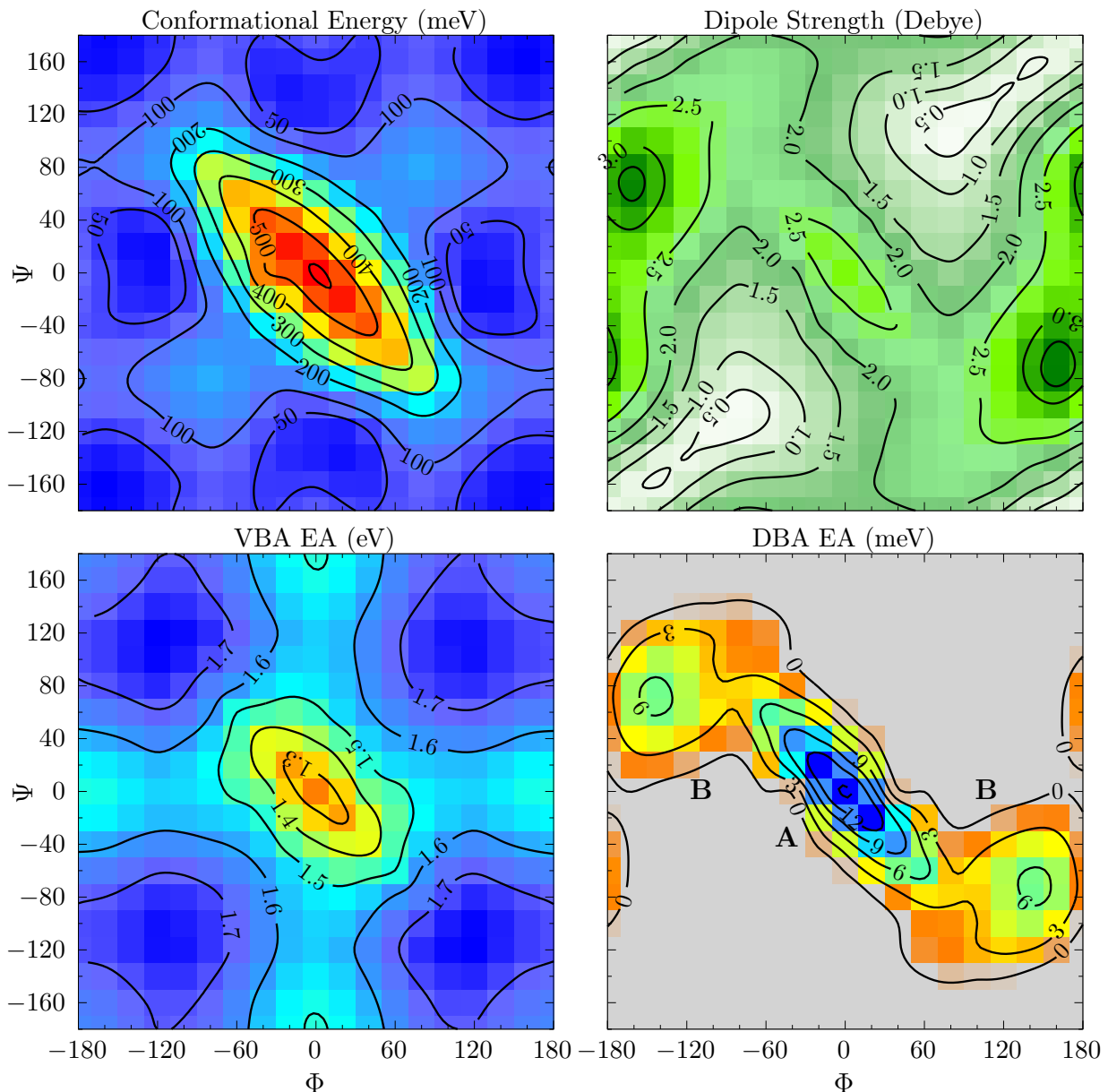


Figure 4.3: Surfaces of Q0. From left to right and top to bottom: potential energy surface (CC2), dipole strength surface (DFT TPSS), PES for the VBS (EA-EOM-CC2), and PES for the DBS (EA-EOM-CC2). Gray points the DBS surface indicate that the DBS is not predicted to exist.

only five points exhibiting binding energies up to 2 meV. Region B in Figure 4.3, centred at $(\pm 140, \mp 20)$ ($\mu = 3.2$ D), is larger and reaches a maximum binding energy of 6.2 meV. Region A, at $(0,0)$, is the most strongly bound, with a maximum of 15.8 meV, despite its lower dipole strength. This may be attributed to the orientation of the dipole moment: in region B, the dipole points above the quinone, and the DBS electron density interacts repulsively with the π system, whereas in region A, the dipole is directed away from the quinone plane. In Figure 4.4, these cases are shown.

Surprisingly, CC2 predicts DBSs in region A supported by dipole moments as small as 1.6D, which is significantly lower than the commonly cited threshold of 2.5D and falls within the range of the ideal dipole DBS⁸. This result suggests that, in addition to the excess electron density being spatially separated from the valence electrons, further stabilisation arises from dispersion interactions with the π system. Effects similar to this have been experimentally observed in indolide anions¹¹⁵. Nevertheless, the high conformational energy of region A makes its population unlikely.

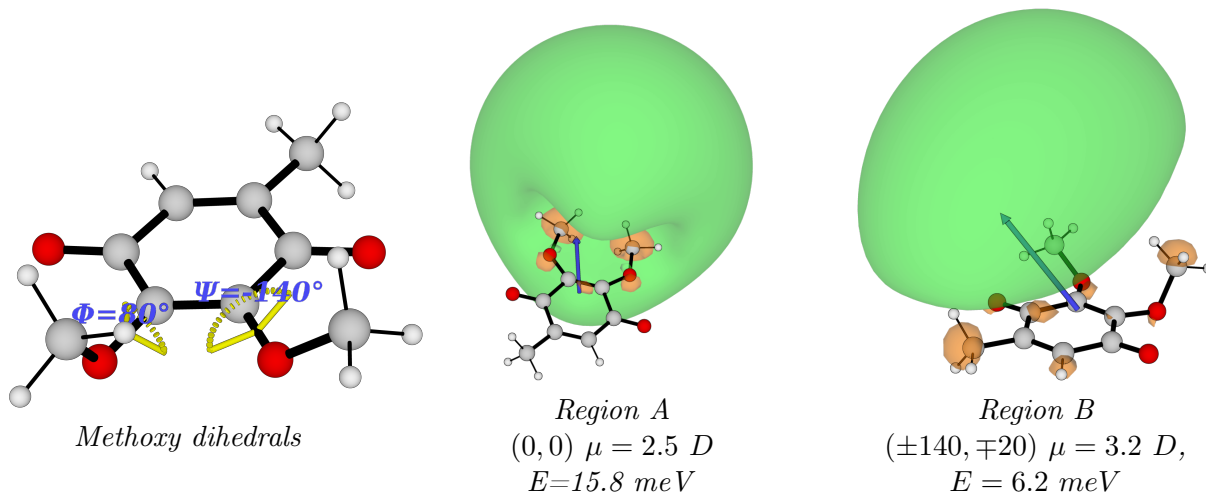


Figure 4.4: Dyson orbitals of Q0 calculated with RI-EA-EOM-CC2/aug-cc-pVDZ+6s3p. The left panel explicitly shows the methoxy dihedral coordinates. The middle panel shows the Dyson orbital of the strongest bound DBS from region B. The right panel shows the Dyson orbital strongest bound DBS from region A. The isosurface is set to 0.005 a.u. and the dipole moment vector is shown as a green arrow with origin at the centre of mass.

Surfaces of Q1

The isoprene tail introduces additional degrees of freedom, resulting in a more complex conformational landscape. To investigate its effect, the analogous surfaces for Q₁ were constructed by fixing the bend and dihedral angles of the isoprene unit relative to the quinone plane. The frozen values of said angles were taken from the crystal structure

of the quinone in the active site of bacterial complex I (PDB: 6I0D)⁷⁴, as presented in Figure 4.6. The results are shown in Figure 4.5. In this case, the molecule has no plane of symmetry and all points of the surface have to be sampled. The PES and dipole surfaces were calculated with DFT using the TPSS functional. Due to the computational cost, only the points with a dipole strength above 1.6 Debye were sampled.

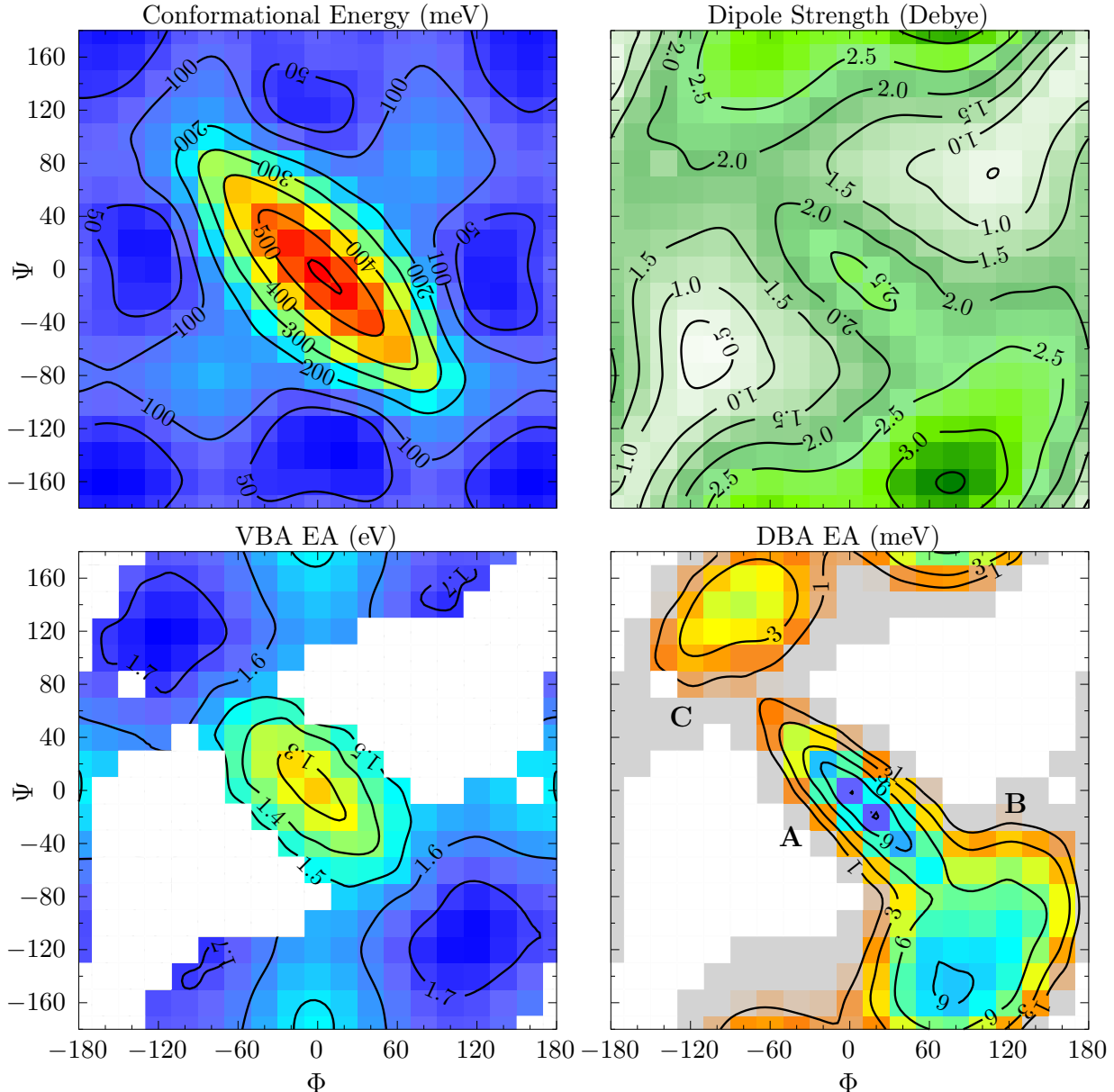


Figure 4.5: Surfaces of Q1. From left to right and top to bottom: potential energy surface (CC2), dipole strength surface (DFT TPSS), PES for the VBS (EA-EOM-CC2), and PES for the DBS (EA-EOM-CC2). White points in VBS and DBS surfaces were not sampled, and gray points the DBS surface indicate that the DBS is not predicted to exist.

Concerning the conformational potential energy surface (PES), the fixed position of the isoprene tail, distant from the quinone moiety, prevents interaction with the methoxy

chains. This renders the scenario largely analogous to that of Q_0 . Steric hindrances would be anticipated with longer tails or alternative configurations. However, the relevance of this particular system is questionable, as crystallographic data¹¹³ indicate that the isoprene tail does not penetrate the quinone moiety's pocket. Within a protein, the orientation of the methoxy chains is dictated by the local environment, with specific configurations favoured by interactions with first-shell amino acids.

The interpretation of the dipole strength surface is also similar to that of Q_0 , with the addition of a fixed dipole originating from the isoprene group, which is oriented approximately out of the plane. This has the effect of dividing region B from Figure 4.3 into two distinct regions for Q_1 , designated B and C. In region B, the local dipole of the isoprene aligns with the methoxy dipoles, resulting in a maximum dipole strength of 3.3 Debye at (160,-80). Conversely, in region C, destructive interference occurs between the local dipoles, leading to a maximum dipole strength of 2.9 Debye at (-60,160). Region A is only slightly affected, retaining a maximum dipole strength of 2.6 D at (0,0).

The VBS surface of Q_1 is more challenging to interpret due to the omitted data points. Nevertheless, the overall picture appears to remain consistent, as the qualitative effect of the rotation of the chains (acting as electron donor or acceptor) is unchanged. The range of vertical electron affinity (VEA) varies surprisingly little, with a global minimum of 1.26 eV at (0,0) and a maximum of 1.76 eV at (-120,120). It had been previously proposed that, contrary to its established spectator role, the isoprene tail might contribute to the stabilisation of the excess electron⁴². However, the results presented herein suggest that the isoprene tail does not significantly affect the VBS of Q_1 , at least in the conformation employed in this study.

Regarding the DBS surface, the impact of the isoprene tail is more pronounced. In region B, where the local dipole of the isoprene tail aligns with the methoxy dipoles, the region expands to encompass a larger area and exhibits a maximum binding energy of 9.1 meV at (80,-160). In region C, the local dipoles interfere destructively, resulting in a smaller area with a maximum binding energy of 5.0 meV at (-80,140). Region A shows a minor difference, with a maximum binding energy of 12.2 meV at (20,-20). In Figure 4.6, the Dyson orbitals of the structures are shown. The variations in electron binding energy in regions B and C can be attributed to changes in the dipole moment strength. The alteration in region A, however, is likely related to a decrease in the favourable interactions between the DBS and the rest of the electronic density, as the dipole moment remains largely unchanged. Similarly to the case with Q_0 , it is noteworthy that structures with dipole moments below 2.5 D are predicted to be bound by EA-EOM-CC2; for example,

with dihedrals of (20,20) and a dipole moment of 1.81 D, the binding energy is 2.2 meV.

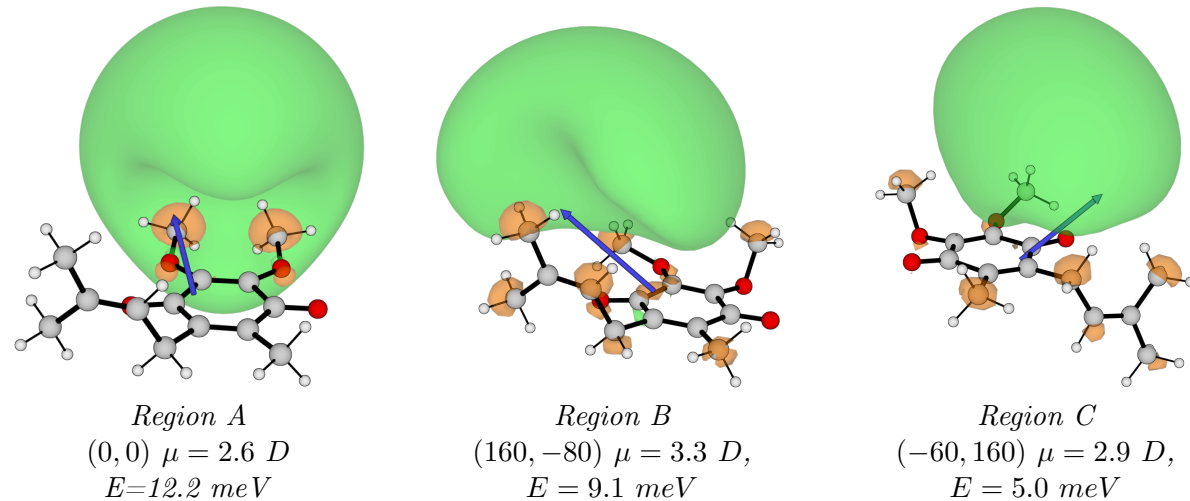


Figure 4.6: Dyson orbitals of Q_0 calculated with RI-EA-EOM-CC2/aug-cc-pVDZ+6s3p. The left panel shows the Dyson orbital of the strongest bound DBS from region A. The middle panel shows the Dyson orbital of the strongest bound DBS from region B. The right panel shows the Dyson orbital of the strongest bound DBS from region A. The isosurface is set to 0.005 a.u. and the dipole moment vector is shown as a blue arrow with origin at the centre of mass.

An important consideration for dipole-bound states (DBS) is the extent of correlation between their binding energy and the strength of the dipole moment that supports them. The DBS maps for Q_0 , Figure 4.3, and Q_1 , Figure 4.5, are clearly demarcated into distinct regions. Figure 4.7 presents a scatter plot illustrating all bound points for both Q_0 and Q_1 . This plot demonstrates that the different regions identified in the maps correspond to separate populations in the scatter plot. A correlation between dipole strength and binding energy is observed in all regions, though the degree of this correlation varies. For instance, region A, which accommodates the strongest dipoles, exhibits a nearly linear relationship between these two parameters for both quinones. This could be interpreted as the molecule acting as an ideal dipole. When comparing region A in Q_0 and Q_1 , the slope for Q_0 is steeper than that for Q_1 , indicating that variations in the chemical environment affect the interplay between the dipole moment and the binding strength.

Concerning the populations in regions B and C, the relationship between the dipole moment and binding energy is considerably less pronounced. This is likely because the DBS occupies a spatial region closer to the other electrons, specifically the π system. In this system, alterations in dipole strength arise from changes in its orientation. Consequently, the displacement of the DBS that accompanies the strengthening of the dipole might result in a less favourable interaction with the remaining electronic density. In general, the electron binding energy is only loosely correlated with the magnitude of the

dipole moment that supports it. However, for analogous systems, such as region A, these two quantities become more significantly interconnected.

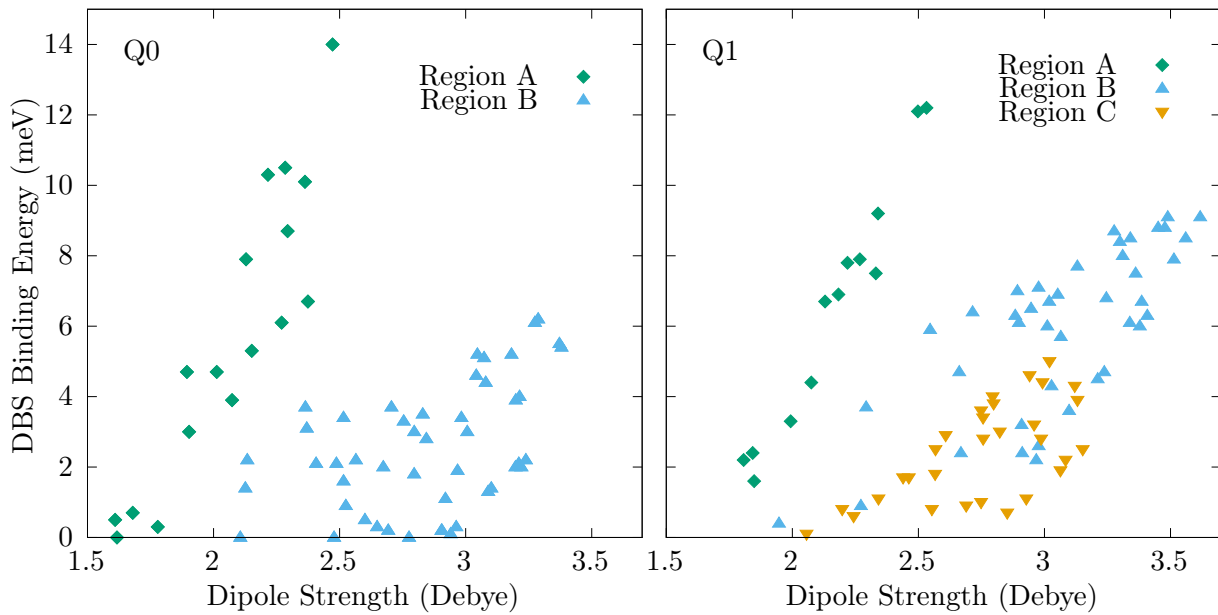


Figure 4.7: Q_0 and Q_1 DBS populations assigned to the DBS surfaces from Figures 4.3 and 4.5.

4.2.2 Interaction with small molecules

Subsequent to the characterisation of the isolated quinones, the focus shifts to the interaction of their anionic states in the presence of small molecules. Recognising that chemical processes in nature do not occur in a vacuum and that environmental interactions are crucial, this work investigates these effects by considering small molecular clusters. Figure 4.8 shows the interactions between Q_0 (region B, $\mu = 3.4$ Debye, $EA_{DBS} = 6$ meV), and selected molecules: methane ($\mu = 0$ Debye), ammonia ($\mu = 1.47$ Debye), water ($\mu = 1.85$ Debye), and hydrogen fluoride ($\mu = 1.82$ Debye). For these model systems, the dipole of the solvent molecule was oriented to interact either constructively or destructively with the quinone's dipole. In the case of methane, which has no dipole moment, it is shown in both cases for comparison. The intermolecular distance was systematically varied from 30 down to 4 Å. The resulting effects on the VBS and DBS energies, are presented in Figure 4.8. It is important to note that none of these molecules support an anionic state on their own. The DBS of a representative $Q_0 +$ water system for each of the two orientations is shown in Figure 4.6.

Considering the DBS, when the solvent and quinone dipoles are opposed, polar molecules induce a wide well with a minimum at around 8 Å. The electron binding energy of the

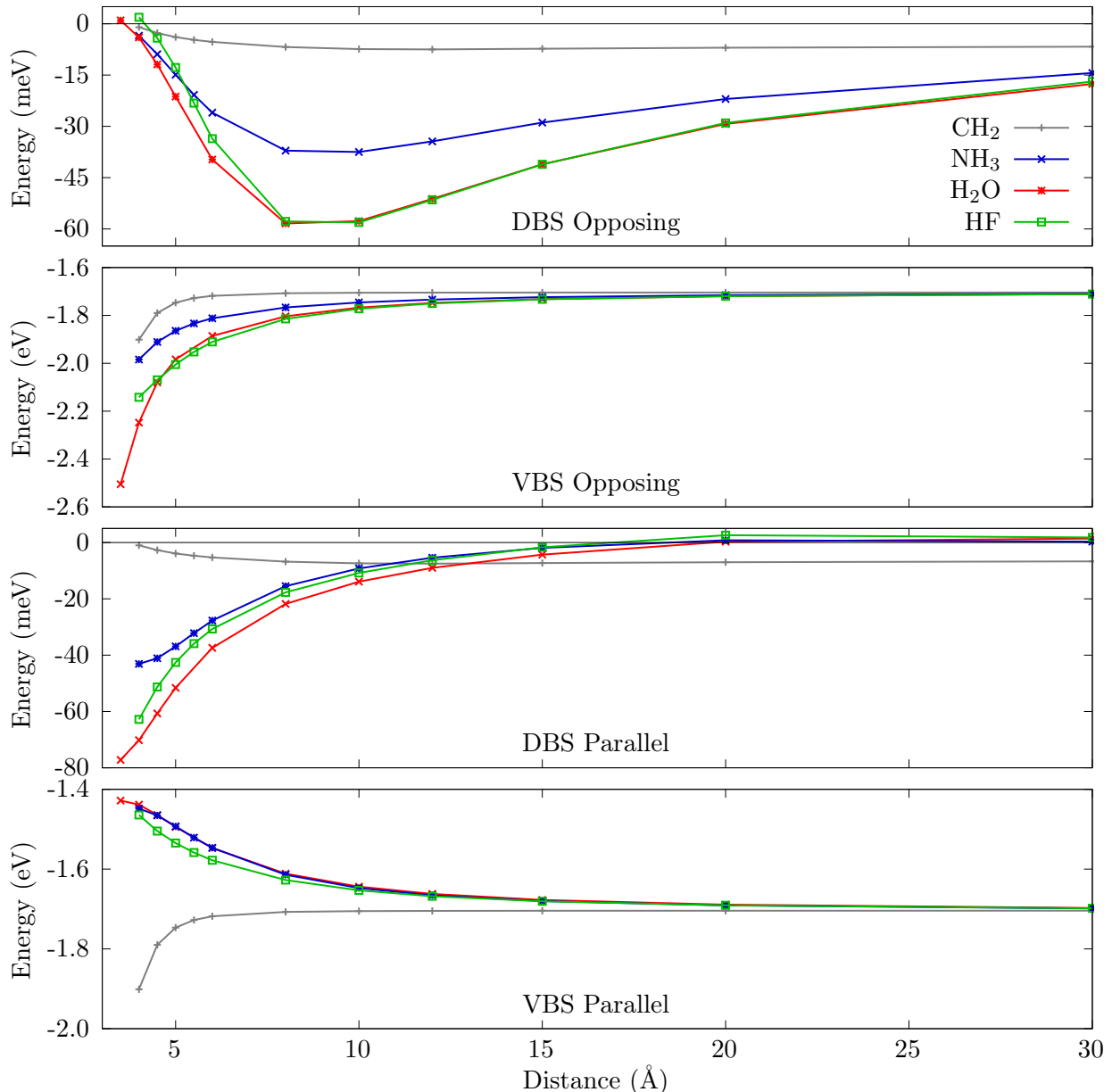


Figure 4.8: Q_0 interaction with small molecules. From top to bottom: DBS with opposing dipoles, VBS with opposing dipoles, DBS with aligned dipoles, and VBS with aligned dipoles.

DBS reaches 60 meV with both water and HF, and 37 meV with ammonia. This represents a more than tenfold increase compared to the 5.4 meV binding energy of the isolated quinone. Stabilisation by methane is considerably weaker, as it arises solely from dispersion forces. The similarity between the water and HF interaction curves is noteworthy; they overlap almost perfectly across most of the separation range. This congruence is attributed to their comparable dipole moments (1.85 D for water; 1.82 D for HF). At large separations, the specific electronic structures of these solvent molecules are less influential, and the DBS primarily experiences the effect of their dipole moments. The interaction with ammonia is weaker due to its smaller dipole moment of 1.47 D. This

scenario is characteristic of a solvated electron within a 'cavity'^{8,57}. At an intermolecular distance of approximately 4 Å, the interaction becomes repulsive for all molecules studied due to steric interactions, causing the DBS to become unbound due to steric hindrance.

Conversely, with parallel dipole orientations, polar molecules exhibit repulsion at large distances. This is attributable to the negative end of the solvent dipole destabilising the DBS. At shorter ranges, however, the local dipoles combine constructively, thereby stabilising the binding energy. For water, which possesses the largest dipole moment, the DBS attains an electron binding energy of 80 meV, with the total system dipole moment being 6.1 Debye. Such configurations have recently been observed in photoelectron spectroscopy experiments²¹ and are thought to play an important role in the transfer of a VBS to a solvated electron.

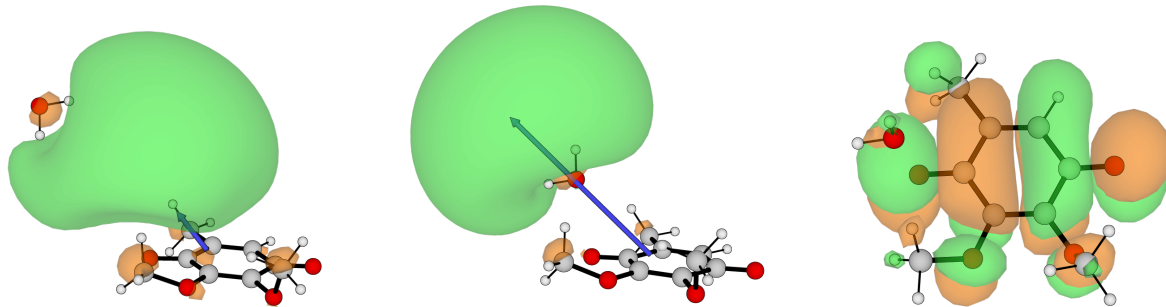


Figure 4.9: Dyson orbitals of Q0 + water calculated with RI-EA-EOM-CC2/aug-cc-pVDZ+6s3p. Left, system where the dipoles are pointing in opposite directions at an intermolecular distance of 8 Å. Middle: dipoles aligned at an intermolecular distance of 4 Å. Right: VBS of Q0 and a water molecule at 4 Å. The isosurface is set to 0.01 a.u. and the dipole moment vector is shown as a blue arrow with origin at the centre of mass.

The interaction also significantly affects the VBS. When the dipoles are opposed, *i.e.*, the positive end of the solvent dipole is oriented towards the excess electronic charge of the quinone, the VBS is strongly stabilised at short intermolecular distances. With water, the VBS achieves a VEA of 2.5 eV, an increase of over 0.8 eV compared to the isolated quinone. A similar effect is observed for HF, yielding a VEA of 2.5 eV, while the stabilisation is less pronounced for ammonia and methane. A comparison of the influence of surrounding molecules on the VBS with that of methoxy chain rotation, as discussed in section 4.2.1, reveals that intermolecular interactions can be considerably more influential. The protein environment has probably a larger effect on the CoQ EA than the orientation adopted by the methoxy chains.

If the dipoles are aligned, the negative end of the solvent dipole interacts with the VBS and is destabilised. A similar and unfavourable trend is observed for the three polar

molecules. At an intermolecular distance of 4 Å, the VEA decreases to approximately 1.4 eV. The destabilisation arises from the negative end of the solvent dipole repelling the excess electron density of the quinone.

Chapter 5

Conclusion and Outlook

This thesis presents a theoretical investigation of anionic states of ubiquinone, which supports both a dipole-bound state and valence-bound states, primarily through equation-of-motion coupled-cluster (EOM-CC) techniques. The principal objectives included benchmarking EOM-CC2-based approaches, assessing basis set considerations for DBSs, implementing of Dyson orbitals for EOM-CC2, and applying these methods to ubiquinone (CoQ) analogues, Q_0 and Q_1 .

Scrutiny of basis set dependence for EA-EOM-CC2 revealed that, although larger cardinality sets (e.g. aug-cc-pVTZ) are often beneficial, the inclusion sufficiently diffuse functions is critical for describing the spatial extension of DBS orbitals. In general CC2 tends to overbind these states when compared to CCSD.

For VBSs, EA-EOM-CC2 was benchmarked against known quinones, showing that spin-component scaling (SCS) notably improves accuracy relative to uncorrected CC2. EA-EOM-CC2-SCS tends to slightly underbind the VBS states. However, unscaled CC2 has a consistent error and is able to recover the trends. The diffuse functions integral to DBSs had minimal impact on VBS energies, as they are much more localized in space.

A methodological advance was the implementation of EOM-CC2 Dyson orbitals. Their quality was assessed by comparing them to EOM-CCSD Dyson orbitals and HF orbitals in the calculation of photodetachment cross-sections. Validating EOM-CC2 Dyson orbitals as a resource-efficient alternative to EOM-CCSD.

Investigations of Q_0 revealed the interplay between methoxy chain conformations and the resulting potential energy, dipole moment, VBS, and DBS surfaces. Five minima were detected on the neutral PES, with methoxy group orientations dictating the dipole moment and hence affecting DBS energies.

Extending to Q_1 , the attached isoprene tail altered the overall molecular dipole to create changes in DBS binding, with constructive dipolar alignment enhancing DBS stability and destructive alignment reducing it. The VBS of Q_1 was not particularly sensitive to the isoprene tail's presence. Different modes of DBS stabilization were observed, depending on their interaction with the rest of that electronic density. Within each mode, or region, the DBS binding strength seems to be correlated strongly with dipole magnitude.

Preliminary explorations of interactions between Q_0 and small molecules (methane, ammonia, water, HF) underscored the sensitivity of both VBSs and DBSs to the local environment. This outcome emphasises the importance of considering environmental effects, which is essential to model states in condensed-phase or biological settings.

Overall, this thesis advances the understanding of non-valence anionic states and the computational techniques applied to them. The benchmarking of EA-EOM-CC2 furnishes guidelines for those seeking cost-effective yet reliable estimates of electron affinities, DBSs, and VBSs, while confirming the utility of EOM-CC2 Dyson orbitals in photodetachment studies. The exploration of ubiquinone anion states underscores how molecular conformation and local electrostatic factors govern the stability and character of both VBSs and DBSs. The observation of DBSs supported by smaller dipole moments challenges common assumptions, highlighting the relevance of dispersion-type interactions in NVSs.

From a pedagogical perspective, this work comprehensively spans multiple facets of theoretical chemistry and computational modelling. Starting from the bottom with a derivation of an algebraic expression for EOM-CC2 Dyson orbitals, progresses to their implementation in commercial quantum-chemistry software, and culminates in their application to a sizeable (*bio*)chemical challenge: the anionic states of ubiquinone.

Despite these contributions, several directions for further work remain:

- **Advanced Solvation Models:** Though small-molecule interactions were considered, explicit solvation or hybrid QM/MM simulations could quantitatively characterise environmental influence on VBS and DBS formation in solution or protein settings. Other techniques that could be utilised is electrostatic embedding.
- **Dynamic Effects:** For larger systems that include more solvating molecules, introducing molecular dynamics simulations to account for structural fluctuations would offer insights into anion state energies and interconversions under realistic conditions.

- **Relating to Experimental Observables:** Future efforts could concentrate on predicting and interpreting experimental data, such as electron transmission, photoelectron angular distributions, or connecting VBS/DBS energies to redox properties in electrochemical or biochemical contexts. Specifically, one could compute the nonadiabatic couplings between a potential electron donor state and the VBS and

In summary, this thesis offers a thorough computational analysis of non-valence anions, supplies methodological insights, and delivers a closer characterisation of ubiquinone anion states. These outcomes pave the way for further studies of the complex physics and chemistry associated with such species in larger or more intricate biological frameworks.

Bibliography

- (1) Simons, J. *The Journal of Physical Chemistry A* **2008**, *112*, 6401–6511.
- (2) Simons, J. *The Journal of Physical Chemistry A* **2023**, *127*, 3940–3957.
- (3) Simons, J. *Annual Review of Physical Chemistry* **2011**, *62*, 107–128.
- (4) Herbert, J. M. *Reviews in Computational Chemistry Volume 28* **2015**, 391–517.
- (5) Fermi, E.; Teller, E. *Physical Review* **1947**, *72*, 399.
- (6) Desfrançois, H. *Int. J. Mod. Phys. B* **1996**, *10*, 1339.
- (7) Gutowski, M.; Skurski, P.; Boldyrev, A. I.; Simons, J.; Jordan, K. D. *Physical Review A* **1996**, *54*, 1906.
- (8) Jordan, K. D.; Wang, F. *Annual review of physical chemistry* **2003**, *54*, 367–396.
- (9) Qian, C.-H.; Zhu, G.-Z.; Wang, L.-S. *The journal of physical chemistry letters* **2019**, *10*, 6472–6477.
- (10) Jordan, K. D.; Liebman, J. F. *Chemical Physics Letters* **1979**, *62*, 143–147.
- (11) Desfrançois, C.; Bouteiller, Y.; Schermann, J.; Radisic, D.; Stokes, S.; Bowen, K.; Hammer, N.; Compton, R. *Physical review letters* **2004**, *92*, 083003.
- (12) Sommerfeld, T.; Dreux, K. M.; Joshi, R. *The Journal of Physical Chemistry A* **2014**, *118*, 7320–7329.
- (13) Sommerfeld, T.; Bhattacharai, B.; Vysotskiy, V. P.; Cederbaum, L. S. *The Journal of chemical physics* **2010**, *133*.
- (14) Voora, V. K.; Cederbaum, L. S.; Jordan, K. D. *The journal of physical chemistry letters* **2013**, *4*, 849–853.
- (15) Voora, V. K.; Jordan, K. D. *The Journal of Physical Chemistry A* **2014**, *118*, 7201–7205.
- (16) Voora, V. K.; Kairalapova, A.; Sommerfeld, T.; Jordan, K. D. *The Journal of Chemical Physics* **2017**, *147*.
- (17) Schiedt, J.; Weinkauf, R.; Neumark, D. M.; Schlag, E. *Chemical Physics* **1998**, *239*, 511–524.

- (18) Jalbout, A.; Adamowicz, L. *The Journal of Physical Chemistry A* **2001**, *105*, 1033–1038.
- (19) Gutowski, M.; Hall, C.; Adamowicz, L.; Hendricks, J.; De Clercq, H.; Lyapustina, S.; Nilles, J.; Xu, S.-J.; Bowen Jr, K. *Physical review letters* **2002**, *88*, 143001.
- (20) Eustis, S.; Wang, D.; Lyapustina, S.; Bowen, K. H. *The Journal of chemical physics* **2007**, *127*.
- (21) Clarke, C. J.; Michi Burrow, E.; Verlet, J. R. *Nature Communications* **2025**, *16*, 2113.
- (22) Hendricks, J.; Lyapustina, S.; De Clercq, H.; Bowen, K. *The Journal of chemical physics* **1998**, *108*, 8–11.
- (23) Sommerfeld, T. *Physical Chemistry Chemical Physics* **2002**, *4*, 2511–2516.
- (24) Sommerfeld, T. *The Journal of Physical Chemistry A* **2004**, *108*, 9150–9154.
- (25) Sommerfeld, T. In *Journal of Physics: Conference Series*, 2005; Vol. 4, p 245.
- (26) Verlet, J. R.; Anstoter, C. S.; Bull, J. N.; Rogers, J. P. *The Journal of Physical Chemistry A* **2020**, *124*, 3507–3519.
- (27) Kang, D. H.; Kim, J.; Eun, H. J.; Kim, S. K. *Accounts of Chemical Research* **2022**, *55*, 3032–3042.
- (28) Hassan, S. Z.; Tauch, J.; Kas, M.; Nötzold, M.; Carrera, H. L.; Endres, E. S.; Wester, R.; Weidemüller, M. *Nature communications* **2022**, *13*, 818.
- (29) Fortenberry, R. C. *The Journal of Physical Chemistry A* **2015**, *119*, 9941–9953.
- (30) Gu, J.; Leszczynski, J.; Schaefer III, H. F. *Chemical reviews* **2012**, *112*, 5603–5640.
- (31) Narayanan SJ, J.; Tripathi, D.; Verma, P.; Adhikary, A.; Dutta, A. K. *ACS omega* **2023**, *8*, 10669–10689.
- (32) Sedmidubská, B.; Kočíšek, J. *Physical Chemistry Chemical Physics* **2024**, *26*, 9112–9136.
- (33) Desfrançois, C. *Physical Review A* **1995**, *51*, 3667.
- (34) Liu, G.; Ciborowski, S. M.; Graham, J. D.; Buptyndyk, A. M.; Bowen, K. H. *The Journal of Chemical Physics* **2020**, *153*.
- (35) Rogers, J. P.; Anstoöter, C. S.; Bull, J. N.; Curchod, B. F.; Verlet, J. R. *The Journal of Physical Chemistry A* **2019**, *123*, 1602–1612.
- (36) Clarke, C. J.; Verlet, J. R. *Annual Review of Physical Chemistry* **2024**, *75*.
- (37) Cyr, D. R.; Hayden, C. C. *The Journal of chemical physics* **1996**, *104*, 771–774.
- (38) Neumark, D. M. *Annual review of physical chemistry* **2001**, *52*, 255–277.

- (39) Carles, S.; Desfrançois, C.; Schermann, J.; Berges, J.; Houée-Levin, C. *International Journal of Mass Spectrometry* **2001**, *205*, 227–232.
- (40) Bradforth, S. E.; Jungwirth, P. *The Journal of Physical Chemistry A* **2002**, *106*, 1286–1298.
- (41) Ameixa, J.; Arthur-Baidoo, E.; Pereira-da-Silva, J.; Ončák, M.; Ruivo, J.; Varella, M. d. N.; Da Silva, F. F.; Denifl, S. *Computational and Structural Biotechnology Journal* **2023**, *21*, 346–353.
- (42) Pshenichnyuk, S. A.; Modelli, A.; Asfandiarov, N. L.; Komolov, A. S. *The Journal of chemical physics* **2020**, *153*.
- (43) Skurski, P.; Gutowski, M.; Simons, J. *International Journal of Quantum Chemistry* **2000**, *80*, 1024–1038.
- (44) Thiam, G.; Rabilloud, F. *Journal of Chemical Theory and Computation* **2023**, *19*, 2842–2849.
- (45) Vila, F. D.; Jordan, K. D. *The Journal of Physical Chemistry A* **2002**, *106*, 1391–1397.
- (46) Ivanov, A. S.; Zhang, X.; Wang, H.; Boldyrev, A. I.; Ganteför, G.; Bowen, K. H.; Cernusak, I. *The Journal of Physical Chemistry A* **2015**, *119*, 11293–11303.
- (47) Moorby, R. E.; Parravicini, V.; Alessio, M.; Jagau, T.-C. *Physical Chemistry Chemical Physics* **2024**, *26*, 6532–6539.
- (48) Haldar, S.; Dutta, A. K. *The Journal of Physical Chemistry A* **2020**, *124*, 3947–3962.
- (49) Schulz, C. E.; Dutta, A. K.; Izsák, R.; Pantazis, D. A. *Journal of Computational Chemistry* **2018**, *39*, 2439–2451.
- (50) Christiansen, O.; Koch, H.; Jørgensen, P. *Chemical Physics Letters* **1995**, *243*, 409–418.
- (51) Paran, G. P.; Utku, C.; Jagau, T.-C. *Physical Chemistry Chemical Physics* **2024**, *26*, 1809–1818.
- (52) Coe, J.; Lee, G.; Eaton, J.; Arnold, S.; Sarkas, H.; Bowen, K.; Ludewigt, C.; Haberland, H.; Worsnop, D. *The Journal of chemical physics* **1990**, *92*, 3980–3982.
- (53) Verlet, J.; Bragg, A.; Kammerath, A.; Cheshnovsky, O.; Neumark, D. *Science* **2005**, *307*, 93–96.
- (54) Coe, J. V.; Williams, S. M.; Bowen, K. H. *International Reviews in Physical Chemistry* **2008**, *27*, 27–51.

- (55) Siefermann, K. R.; Liu, Y.; Lugovoy, E.; Link, O.; Faubel, M.; Buck, U.; Winter, B.; Abel, B. *Nature chemistry* **2010**, *2*, 274–279.
- (56) Kumar, A.; Walker, J. A.; Bartels, D. M.; Sevilla, M. D. *The Journal of Physical Chemistry A* **2015**, *119*, 9148–9159.
- (57) Herbert, J. M. *Physical Chemistry Chemical Physics* **2019**, *21*, 20538–20565.
- (58) Herbert, J. M.; Coons, M. P. *Annual review of physical chemistry* **2017**, *68*, 447–472.
- (59) Kevan, L. *Accounts of Chemical Research* **1981**, *14*, 138–145.
- (60) Anusiewicz, I.; Skurski, P.; Simons, J. *The Journal of Physical Chemistry A* **2020**, *124*, 2064–2076.
- (61) Castellani, M. E.; Anstöter, C. S.; Verlet, J. R. *Physical Chemistry Chemical Physics* **2019**, *21*, 24286–24290.
- (62) Larsen, R. E.; Glover, W. J.; Schwartz, B. J. *Science* **2010**, *329*, 65–69.
- (63) Narayanan SJ, J.; Verma, P.; Adhikary, A.; Kumar Dutta, A. *ChemPhysChem* **2024**, *25*, e202400581.
- (64) Chen, H.-Y.; Sheu, W.-S. *Journal of the American Chemical Society* **2000**, *122*, 7534–7542.
- (65) Messina, F.; Bräm, O.; Cannizzo, A.; Chergui, M. *Nature communications* **2013**, *4*, 2119.
- (66) Carter-Fenk, K.; Johnson, B. A.; Herbert, J. M.; Schenter, G. K.; Mundy, C. J. *The journal of physical chemistry letters* **2023**, *14*, 870–878.
- (67) Mitchell, P. *Nature* **1961**, *191*, 144–148.
- (68) Wikstrom, M. K. *Nature* **1977**, *266*, 271–273.
- (69) Rutledge, H. L.; Tezcan, F. A. *Chemical reviews* **2020**, *120*, 5158–5193.
- (70) Gray, H. B.; Winkler, J. R. *Annual review of biochemistry* **1996**, *65*, 537–561.
- (71) Blumberger, J. *Chemical reviews* **2015**, *115*, 11191–11238.
- (72) Ernster, L.; Dallner, G. *Biochimica et Biophysica Acta (BBA)-Molecular Basis of Disease* **1995**, *1271*, 195–204.
- (73) Vasconcellos, F. *Wikimedia Commons* **2007**.
- (74) Gutiérrez-Fernández, J.; Kaszuba, K.; Minhas, G. S.; Baradaran, R.; Tambalo, M.; Gallagher, D. T.; Sazanov, L. A. *Nature communications* **2020**, *11*, 4135.
- (75) Russell, W. J. *Chemical News and Journal of Physical Science* **1873**, *28*, 148–153.

- (76) **2025.**
- (77) Chen, J.; Pelc, A.; Ameixa, J.; Kossoski, F.; Denifl, S. *ACS omega* **2024**, *9*, 38032–38043.
- (78) Bull, J. N.; West, C. W.; Verlet, J. R. *Physical Chemistry Chemical Physics* **2015**, *17*, 16125–16135.
- (79) West, C. W.; Bull, J. N.; Antonkov, E.; Verlet, J. R. *The Journal of Physical Chemistry A* **2014**, *118*, 11346–11354.
- (80) Nonella, M. *Photosynthesis research* **1998**, *55*, 253–259.
- (81) Gamiz-Hernandez, A. P.; Jussupow, A.; Johansson, M. P.; Kaila, V. R. *Journal of the American Chemical Society* **2017**, *139*, 16282–16288.
- (82) Hartree, D. R. In *Mathematical Proceedings of the Cambridge Philosophical Society*, 1928; Vol. 24, pp 111–132.
- (83) Fock, V. *Zeitschrift für Physik* **1930**, *61*, 126–148.
- (84) Szabo, A.; Ostlund, N. S., *Modern quantum chemistry: introduction to advanced electronic structure theory*; Courier Corporation: 1996.
- (85) Shavitt, I.; Bartlett, R. J., *Many-body methods in chemistry and physics: MBPT and coupled-cluster theory*; Cambridge university press: 2009.
- (86) Grimme, S. *The Journal of chemical physics* **2003**, *118*, 9095–9102.
- (87) Hohenberg, P.; Kohn, W. *Phys. Rev* **1964**, *136*, B864.
- (88) Kohn, W.; Sham, L. J. *Physical review* **1965**, *140*, A1133.
- (89) Sherrill, C. D.; Schaefer III, H. F. In *Advances in quantum chemistry*; Elsevier: 1999; Vol. 34, pp 143–269.
- (90) Bartlett, R. J.; Purvis, G. D. *International Journal of Quantum Chemistry* **1978**, *14*, 561–581.
- (91) Pople, J. A.; Binkley, J. S.; Seeger, R. *International Journal of Quantum Chemistry* **1976**, *10*, 1–19.
- (92) Čížek, J. *The Journal of Chemical Physics* **1966**, *45*, 4256–4266.
- (93) Čížek, J. *Advances in chemical physics* **1969**, *14*, 35–89.
- (94) Monkhorst, H. J. *International Journal of Quantum Chemistry* **1977**, *12*, 421–432.
- (95) Raghavachari, K.; Trucks, G. W.; Pople, J. A.; Head-Gordon, M. *Chemical Physics Letters* **1989**, *157*, 479–483.
- (96) Hättig, C.; Weigend, F. *The Journal of Chemical Physics* **2000**, *113*, 5154–5161.

- (97) Shaalan Alag, A.; Jelenfi, D. P.; Tajti, A.; Szalay, P. G. *Journal of Chemical Theory and Computation* **2022**, *18*, 6794–6801.
- (98) Emrich, K. *Nuclear Physics A* **1981**, *351*, 379–396.
- (99) Stanton, J. F.; Bartlett, R. J. *The Journal of chemical physics* **1993**, *98*, 7029–7039.
- (100) Krylov, A. I. *Annu. Rev. Phys. Chem.* **2008**, *59*, 433–462.
- (101) Jagau, T.-C.; Krylov, A. I. *The Journal of chemical physics* **2016**, *144*.
- (102) Melania Oana, C.; Krylov, A. I. *The Journal of chemical physics* **2007**, *127*.
- (103) Epifanovsky, E. et al. *J. Chem. Phys.* **2021**, *155*, 084801.
- (104) Dunning Jr, T. H. *The Journal of chemical physics* **1989**, *90*, 1007–1023.
- (105) Gozem, S.; Krylov, A. I. *Wiley Interdisciplinary Reviews: Computational Molecular Science* **2022**, *12*, e1546.
- (106) Gozem, S.; Krylov, A. I. *Chem. Lett.* **2015**, *6*, 4532–4540.
- (107) Tao, J.; Perdew, J. P.; Staroverov, V. N.; Scuseria, G. E. *Physical review letters* **2003**, *91*, 146401.
- (108) Grimme, S.; Ehrlich, S.; Goerigk, L. *Journal of computational chemistry* **2011**, *32*, 1456–1465.
- (109) Zheng, J.; Xu, X.; Truhlar, D. G. *Theoretical Chemistry Accounts* **2011**, *128*, 295–305.
- (110) Weigend, F.; Ahlrichs, R. *Physical Chemistry Chemical Physics* **2005**, *7*, 3297–3305.
- (111) Díaz-Tinoco, M.; Corzo, H. H.; Pawłowski, F.; Ortiz, J. *Molecular Physics* **2019**, *117*, 2275–2283.
- (112) Taguchi, A. T.; Mattis, A. J.; O’Malley, P. J.; Dikanov, S. A.; Wraight, C. A. *Biochemistry* **2013**, *52*, 7164–7166.
- (113) Taguchi, A. T.; O’Malley, P. J.; Wraight, C. A.; Dikanov, S. A. *Biochemistry* **2013**, *52*, 4648–4655.
- (114) De Almeida, W. B.; Taguchi, A. T.; Dikanov, S. A.; Wraight, C. A.; O’Malley, P. J. *The journal of physical chemistry letters* **2014**, *5*, 2506–2509.
- (115) Yuan, D.-F.; Liu, Y.; Zhang, Y.-R.; Wang, L.-S. *Journal of the American Chemical Society* **2023**, *145*, 5512–5522.

Appendix A

Algebraic Expressions for the Dyson Orbitals

EOM-EA-CC Dyson orbitals

Right EOM-EA-CC Dyson orbital, $\phi_D^{EA,R} = \sum_i^{\text{occ}} \gamma_i^{EA,R} \phi_i + \sum_a^{\text{vir}} \gamma_a^{EA,R} \phi_a$:

$$\gamma_i^{EA,R} = \langle EA | \hat{a}_i^\dagger | CC \rangle \quad (1)$$

$$= l_a \quad (2)$$

$$\begin{aligned} \gamma_a^{EA,R} &= \langle EA | \hat{a}_a^\dagger | CC \rangle \\ &= - \sum_c t_{ic} l_c - \frac{1}{2} \sum_{kcd} t_{ki}^{dc} l_{dc}^k \end{aligned} \quad (3)$$

Left EOM-EA-CC Dyson orbital, $\phi_D^{EA,L} = \sum_i^{\text{occ}} \gamma_i^{EA,L} \phi_i + \sum_a^{\text{vir}} \gamma_a^{EA,L} \phi_a$:

$$\begin{aligned} \gamma_i^{EA,L} &= \langle CC | \hat{a}_i | EA \rangle \\ &= - \sum_c \lambda_{ic} r_c - \frac{1}{2} \sum_{kcd} \lambda_{ik}^{cd} r_k^{dc} \end{aligned} \quad (4)$$

$$\begin{aligned} \gamma_a^{EA,L} &= \langle CC | \hat{a}_a | EA \rangle \\ &= r_a + \sum_{kc} \lambda_{kc} r_{ca}^k + \sum_k \gamma_k^{EA,L} t_{ka} - \frac{1}{2} \sum_{klcd} \lambda_{lk}^{dc} t_{lk}^{da} r_c \end{aligned} \quad (5)$$

EOM-EA-EE-CC Dyson orbitals

Right Dyson orbital, $\phi_D^{EA-EE,R} = \sum_i^{\text{occ}} \gamma_i^{EA-EE,R} \phi_i + \sum_a^{\text{vir}} \gamma_a^{EA-EE,R} \phi_a$:

$$\begin{aligned}\gamma_i^{\text{EA-EE,R}} &= \langle EA | \hat{a}_i^\dagger | EE \rangle \\ &= r_0 \gamma_a^{\text{EA,R}} - \sum_c r_{ic} l_c - \frac{1}{2} \sum_{lcd} r_{il}^{cd} l_{dc}^l - \sum_{lcd} l_{dc}^l t_{ic} r_{ld}\end{aligned}\quad (6)$$

$$\begin{aligned}\gamma_a^{\text{EE-EA,R}} &= \langle EA | \hat{a}_a^\dagger | EE \rangle \\ &= r_0 l_a + \sum_{kc} l_{ca}^k r_{kc}\end{aligned}\quad (7)$$

Left Dyson orbital, $\phi_D^{\text{EE-EA,L}} = \sum_i^{\text{occ}} \gamma_i^{\text{EE-EA,L}} \phi_i + \sum_a^{\text{vir}} \gamma_a^{\text{EE-EA,L}} \phi_a$:

$$\begin{aligned}\gamma_i^{\text{EE-EA,L}} &= \langle EE | \hat{a}_i | EA \rangle \\ &= - \sum_c l_{ic} r_c - \frac{1}{2} \sum_{kcd} l_{ik}^{cd} r_k^{dc}\end{aligned}\quad (8)$$

$$\begin{aligned}\gamma_a^{\text{EE-EA,L}} &= \langle EE | \hat{a}_a | EA \rangle \\ &= \sum_{kc} l_{kc} r_{ca}^k + \sum_k \gamma_k^{\text{EE-EA,L}} t_{ka} - \frac{1}{2} \sum_{klcd} l_{lk}^{dc} t_{lk}^{da} r_c\end{aligned}\quad (9)$$

EOM-IP-CC Dyson orbitals

Right Dyson orbital, $\phi_D^{\text{IP,R}} = \sum_i^{\text{occ}} \gamma_i^{\text{IP,R}} \phi_i + \sum_a^{\text{vir}} \gamma_a^{\text{IP,R}} \phi_a$:

$$\begin{aligned}\gamma_a^{\text{IP,R}} &= \langle CC | \hat{a}_a^\dagger | IP \rangle \\ &= \lambda_{ka} r_k + \frac{1}{2} \lambda_{lk}^{ca} r_{klc}\end{aligned}\quad (10)$$

$$\begin{aligned}\gamma_i^{\text{IP,R}} &= \langle CC | \hat{a}_i^\dagger | IP \rangle \\ &= r_i + \sum_{kc} \lambda_{kc} r_{ik}^c - \sum_c \gamma_c^{\text{IP,R}} t_{ic} - \frac{1}{2} \sum_{klcd} \lambda_{lk}^{dc} t_{li}^{dc} r_k\end{aligned}\quad (11)$$

Left Dyson orbital, $\phi_D^{\text{IP,L}} = \sum_i^{\text{occ}} \gamma_i^{\text{IP,L}} \phi_i + \sum_a^{\text{vir}} \gamma_a^{\text{IP,L}} \phi_a$:

$$\begin{aligned}\gamma_i^{\text{IP,L}} &= \langle IP | \hat{a}_i | CC \rangle \\ &= l_i\end{aligned}\quad (12)$$

$$\begin{aligned}\gamma_a^{\text{IP,L}} &= \langle IP | \hat{a}_a | CC \rangle \\ &= \sum_k t_{ka} l_k + \frac{1}{2} \sum_{klc} t_{kl}^{ac} l_{kl}^c\end{aligned}\quad (13)$$

EOM-EE-IP-CC Dyson orbitals

Right Dyson orbital, $\phi_D^{\text{EE-IP,R}} = \sum_i^{\text{occ}} \gamma_i^{\text{EE-IP,R}} \phi_i + \sum_a^{\text{vir}} \gamma_a^{\text{EE-IP,R}} \phi_a$:

$$\begin{aligned}\gamma_i^{\text{EE-IP,R}} &= \langle EE | \hat{a}_i^\dagger | IP \rangle \\ &= \sum_{kc} l_{kc} r_{ik}^c - \sum_c \gamma_c^{\text{IP-EI}} t_{ic} - \frac{1}{2} \sum_{klcd} l_{lk}^{dc} t_{li}^{dc} r_k\end{aligned}\quad (14)$$

$$\begin{aligned}\gamma_a^{\text{EE-IP,R}} &= \langle EE | \hat{a}_a^\dagger | IP \rangle \\ &= l_{ka} r_k + \frac{1}{2} l_{lk}^{ca} r_{klc}\end{aligned}\quad (15)$$

Left Dyson orbital, $\phi_D^{\text{IP-EE,L}} = \sum_i^{\text{occ}} \gamma_i^{\text{IP-EE,L}} \phi_i + \sum_a^{\text{vir}} \gamma_a^{\text{IP-EE,L}} \phi_a$:

$$\begin{aligned}\gamma_i^{\text{IP-EE,L}} &= \langle IP | \hat{a}_i | EE \rangle \\ &= r_0 l_i + \sum_{kc} l_{ik}^c r_{kc}\end{aligned}\quad (16)$$

$$\begin{aligned}\gamma_a^{\text{IP-EE,L}} &= \langle IP | \hat{a}_a | EE \rangle \\ &= r_0 \gamma_a^{\text{IP,L}} + \sum_k r_{ka} l_k + \frac{1}{2} \sum_{klc} r_{kl}^{ac} l_{kl}^c + \sum_{klc} l_{kl}^c t_{ka} r_{cl}\end{aligned}\quad (17)$$

Appendix B

Photoelectron Cross-sections

TODO: add all gnuplot figures.

Quantum Chemistry and Physical Chemistry

Celestijnenlaan 200F bus 2404

3001 LEUVEN, BELGIË

tel. + 32 16 37 21 98

jeremy.harvey@kuleuven.be

www.kuleuven.be

